

ASH UTILIZATION WITH SILICA AND METALS RECOVERY

Sol Shcherban

The International Association of Sciences, Inc., 110 Bennett Ave., # 3H
New York, NY 10033

Keywords: coal fly ash, utilization, silica and metals recovery

ABSTRACT

The annual generation of electric power in the United States results in production of over 43 million tons of fly ash. Only about 22% of this amount is presently utilized. Neither of the used ash applications requires the recovery of metals and other valuable components (i). In the process of studying, there is another group of methods based on direct recovery of metals from ash (ii). This paper continues presentation of new technologies for ash processing with silica pre-extraction process (SP-process) and recovery of metals. Silica in ash represent about 40-65% of the total, therefore the possibility of silica recovering and converting into a wide variety of pure chemical silicate products with the predetermined properties is one of the main advantages of new technologies. For technical and economic features these perspective technologies present the third new group of methods of ash utilization (iii).

INTRODUCTION

In 1993, approximately 43.4 million metric tons of coal combustion fly ash were produced by the electric utilities in the United States [1]. Only about 22% of this amount was used mainly for cement, concrete products, and other [2]. For these applications, ash is used in an unsophisticated way without recovery of same components (i). The low level of ash utilization shows that such applications are insufficient for the complete utilization of fly ash, which is why there is a constant need for finding new ways to increase utilization of fly ash. For a significant increase in ash utilization, it is necessary to expand the assortment of useful products which can be produced from ash.

Aluminum is one of the major ash components. Many chemo-metallurgical methods were proposed for recovery of alumina from high-silica alumina-containing ores and industrial by-products including ashes (ii). As applied to ashes, these methods have two fundamentally important deficiencies which make them non- or low- profitable. One of them consists of great outlet streams of raw materials and intermediate products which leads to high capital and operating costs of alumina production [3-5]. As it will be shown below, no less important is the second deficiency - withdrawal of silica from the technological process in the form of solid residue. Conversion of silica into solid residue restricts the possibility of its utilization while silica represents the largest component of ash (40-65% of the total).

This paper continues to present new technologies for ash processing which makes it possible to reduce the outlet streams of raw materials and intermediate products, and to put out the most part of silica in the form of chemical silicate products (iii). The earlier papers described the background and main operations of new technologies [6,7]. The purpose of this paper is to expose main features of new technologies with silica pre-extraction process and to evaluate their possible influence on the economic showings.

EXPERIMENTAL

Object of research.

It is important to distinguish the varieties of ashes for choosing methods of the metal recovery, depending on chemical and mineralogical compositions of ash. As object of present consideration, ashes with low content of calcium and magnesium compounds were chosen. Ashes of some typical United States' coals of West Virginia, Ohio, and Illinois as well as ashes of Ekibastuz (Kazakhstan, Russia), Donetzk, Kuznetzk, Podmoscow (Ukraine and Russia) coals are suitable for this consideration. The chemical analysis of ashes and traditional raw materials used by aluminum industry are given in Table 1.

Prospects for ash using for alumina production. Strategy.

There are serious reasons to be doubtful about prospects of ashes to compete with traditional aluminum raw materials if ash is used as a monomineral material like bauxite for aluminum production only. The comparatively low content of alumina, high content of silica, and presence of aluminum mainly in the form of chemically stable mullite [6,7] result in great outlet streams of materials which have to be processed by the most power-consuming operations as roasting, sintering, and other (Table 2). Finally, this leads to the high capital and operating costs of alumina production from ash [3-5].

However, available industrial experience of alumina production shows that high silica materials can be processed profitably if they are used as polymineral raw materials for production of alumina and salable by-products as soda, potash and alkali for nephelines or sulfates for alunites. But ashes do not contain any considerable quantities of alkali (Table 1) whose availability creates a profitable technology of nephelines processing. Therefore, silica- the largest component of ash, can be used as a salable by- product for ashes. The foregoing shows:

- ash can not be processed profitably as a monomineral raw material used for aluminum production only
- to make aluminum production competitive, it is necessary to utilize silica that represents the largest component of the ash
- it is important to develop less power-consuming technologies by means of lowering outlet streams of raw materials and intermediate products.

Methods of ash utilization

Taking into account the principal importance of silica utilization, it is useful to examine all of the methods from the viewpoint of silica recovery and utilization. From this standpoint, all of the methods can be subdivided into three groups (Figure 1):

- (i) Ash uses without recovery of components from ash (cement, concrete products, road base and subbase, structural fills, embankments, filler, grouting, waste stabilization and other)[2].
- (ii) Direct metallurgical processing of ash for alumina (aluminum) production without recovery of silica.
- (iii) Ash processing with silica recovery and utilization [6,7].

Chemo-metallurgical methods of the group (ii).

Many methods of this group are known for recovering aluminum from high-silica alumina containing ores, concentrates, and industrial by-products. Technically suitable for ashes are those that allow to convert the compounds of aluminum, mainly mullite or metakaolinite (in low-temperature formed ashes) into acid- or alkali- soluble compounds by roasting, sintering or high-temperature hydrochemical processes [3-5].

Acid methods

One of the main advantages of acid methods is the possibility of separating the great quantities of silica in the beginning of process by leaching. But this very important advantage can be realized only in the process of direct acid leaching which is suitable for low-temperature formed ashes containing aluminum in the form of metakaolinite. In other methods, the great outlet streams of ash and auxiliary agents (limestone[8], lime, acid or other) have to be sent to the most power-consuming roasting and sintering processes which proceed to the process of leaching (Figure 1 /i/).

Alkaline methods

The current world aluminum production is based only on the alkaline technologies owing to the following advantages of these methods:

- purity and physical properties of alumina correspond to the requirements of the electrolysis process
- comparatively small stream of pulps and liquors because of high solubility of alumina in the solutions
- lack of necessity of corrosion protection for equipment and solution purification from iron

As applied to ashes, the main deficiencies of both acid and alkaline methods are the following:

1. The great streams of ash, furnace charges, cakes, pulps and liquors (Table 2).
2. Withdrawal of silica from technological process in the form of solid residue (Table 3).
Contrary to silica obtained from the silicate solutions, composition and physical properties of solid residue are predetermined by the conditions of leaching therefore they can not be changed. This restricts the areas of solid residue using mainly by cement production. As has been mentioned above this application do not provide the further augmentation of ash utilization.

Ash processing for alumina production with silica recovery and utilization (Figure1, /iii/).

A great difference in solubility of mullite and compounds of free silica (Figure 2) was used for the extraction of the major part of silica from fly ash by silica pre-extraction process (SSP) [6,7]. Silica dissolved in alkaline and soda-alkaline solutions can be converted into a wide variety of valuable pure silicate products (Table 3). Extraction of the largest part of silica from fly ash decreases the outlet streams of ash, limestone, furnace charge, cake, and mud by 1.5-5.0 times (Table 2), and accordingly reduces the capital and operating costs of alumina production from fly ash.

SUMMARY

The major deficiencies of the chemo-metallurgical methods which make them non- or low-profitable for ash processing are the great outlet streams of ash and the intermediate products, and putting out silica in the form of solid residue. The deficiencies can be eliminated by means of new technologies of ash processing with the silica pre-extraction process (SPP). The main advantages of this process can be summarized in the following:

- ash is used as a polymineral source from which all of the major components including alumina, silica and iron [6] can be recovered and utilized
- silica is put out from the technological process in the form of salable chemical silicate products
- the possibility to produce a variety of valuable chemical silicate products becomes a decisive factor for improving economic showings of new technologies
- the major part of silica (50-75%) can be extracted from ash at the beginning of the technological process. This results in outlet streams decreasing and accordingly in reduction of capital and operating costs.

REFERENCES

1. 1993 Coal Combustion Byproducts Production and Consumption, American Coal Ash Association, Inc., Washington, D.C., 1994.
2. Tyson S. and Blackstock T. Coal Combustion Fly Ash - Overview of Applications and Opportunities in the USA. Paper Presented at the 211th ACS National Meeting, New Orleans, LA, March 24-28, 1996, Volume 41, No.2, pp. 587-591.
3. O'Connor D.J. Alumina extraction from non bauxitic materials. Aluminum-Verlag 6mbH, Dusseldorf. p.320-345.
4. Kirbay C., and Barclay J.A. 'Alumina from nonbauxitic resources'. 'Trav. Com. int. etude bauxites, alumine et alum', 1981, No.16, 1-12.
5. Bengston K.B., Chuberka P., Nunn R.F., Phillips W.A., Malm L. and San Jose A.V. 'Some technical and economic comparisons of six processes for the production of alumina from non-bauxitic ores' 'Trav. Com. int. etude bauxites, alumine et alum', 1981, No.16, 109-132.

6. Shcherban S., Rayzman V. and Pevzner I. Technologies of Coal Fly Ash Processing into Metallurgical and Silicate Chemical Products.' Paper Presented at 210th ACS National Meeting Chicago, IL August 20-25, 1995, Volume 40, No.4, pp. 863-867.
7. Shcherban S.A. and Rayzman V.L. 'Alkaline Technologies of Coal Fly Ash Processing into Metallurgical and Silicate Chemical Products', 1995 International Ash Utilization Symposium, October 23-25, Lexington, Kentucky, Proceedings, XI.
8. Torma A.E. 'Extraction of Alumina from Fly Ash', Metal. 37, Jahrgang. Heft 6, June 1983, pp. 589-592.

Table 1. CHEMICAL ANALYSIS OF FLY ASH AND RAW MATERIALS USED BY ALUMINUM INDUSTRY (Wt. %).

Materials	Al ₂ O ₃	SiO ₂	Fe ₂ O ₃	TiO ₂	CaO	MgO	Na ₂ O	K ₂ O
Ash of Ekibastuz coal	28.4	59.6	5.10	1.83	1.31	0.65	0.33	0.59
Ash of WV	30.00	60.00	4.00	1.60	0.60	0.60	0.50	1.50
Bauxite:								
-low silica	41.0-60.0	0.4-8.0	0.3-30	1.0-4.0				
-high silica	43-57	12-19	6-22	2-3.5			Na ₂ O + K ₂ O	
Nepheline Concentrate	28-30	43-44	2-4		2-3		19 - 20	
Nepheline (Russia)	27.5	40-41	4-5			SO ₃	13	
Alunite (Azerbaijan)	22	41	4			20	5	

Table 2. APPROXIMATE OUTLET STREAMS OF RAW MATERIALS AND INTERMEDIATE PRODUCTS DURING PROCESS OF ALUMINA PRODUCTION.

Material	Outlet stream, t/t Al ₂ O ₃		Decreasing of outlet streams, times
	Direct metallurgical ash processing (S-L.S)*	Ash processing with silica preextraction (S-L.S SP)**	
Raw material	3.99 (ash)	2.63 (concentrate)	1.51
Limestone	10.27	2.06	4.98
Furnace charge	15.3	6.26	2.44
Cake	10.00	4.61	2.16
Mud	8.30	2.82	2.94

* S-L.S - soda- limestone sintering process

**S-L.S SP - soda- limestone sintering process with silica pre-extraction

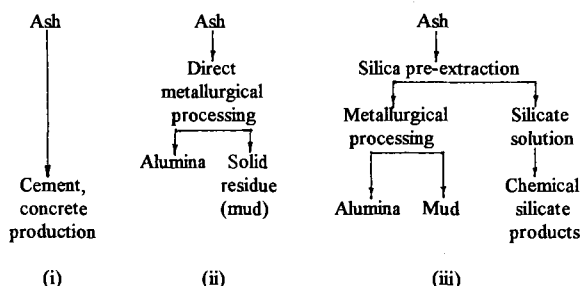


Figure1. Comparison of methods for ash utilization.

(i)-Ash uses without recovery of components. (ii)-Direct metallurgical processing of ash. (iii)-Ash processing with silica pre-extraction.

Table 3. COMPARISON OF SILICON CONTAINING PRODUCTS AND SOLID RESIDUE AFTER ALKALINE PROCESSING OF ASH BY THE DIRECT RECOVERY OF ALUMINA (ii) AND PROCESS WITH SILICA PRE-EXTRACTION (iii).

Method of coal ash processing	Silicon containing products and residue after ash processing		
	Products from solutions	Solid residue. Principal compound	Commercial uses
(ii) Direct recovery of alumina:			
- Lime-Soda Sintering		β - mud (β - Ca_2SiO_4)	cement
- Lime Sintering		β - mud (β - Ca_2SiO_4)	cement
- Hydrochemical high-caustic, high-temperature leaching		calcium-silica mud ($\text{Ca}[\text{H}_2\text{SiO}_4]$)	cement
(iii) Ash processing with silica pre-extraction			
- Sintering with silica pre-extraction process	a) Chemical silicate products*: SAS, SSS, SMS, CMS, SSM, SA, SC and other (45-75% of the SiO_2 total)		glasses, glazes, ceramics, enamels, color cements, zeolite, fillers, plasticizers, cosmetics, detergents and other silicon containing products
		b) β -mud (β - Ca_2SiO_4) (55-25% of the SiO_2 total)	cement

* SAS- silica alkaline solution; SSS- soda-silicate solution; SMC- sodium hydrometasilicate; CMS- calcium hydrometasilicate; SSM- soda-silicate-mixtures; SA- silica amorphous; SC- silica crystalline

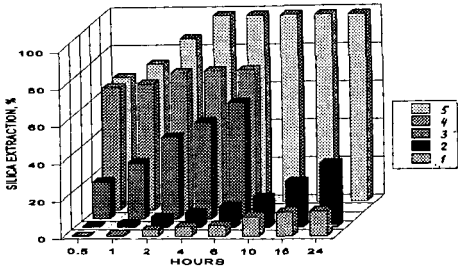


Figure 2. Efficiency of major ash compounds dissolution in alkaline solution: 1-mullite, 2-quartz, 3-ash glassy phase, 4-ash cristobalite, 5-synthetic cristobalite

CHEMICAL VAPOR DEPOSITION: STABLE CARBONS FROM LOW-RANK COALS

Ramesh K. Sharma, Ronald W. Kulas, and Edwin S. Olson
University of North Dakota
Energy & Environmental Research Center
PO Box 9018
Grand Forks, ND 58202

Keywords: Chemical vapor deposition, lignite, activation

ABSTRACT

A chemical vapor deposition (CVD) technique has been used to increase the oxidative stability of activated carbons. Activated carbons prepared from Gascoyne lignite (North Dakota) by thermal or potassium hydroxide activations were subjected to BCl_3 in helium at 727°C with or without benzene for a limited period of time, followed by annealing in helium at 900°C for three days. Untreated and acid-washed coal samples were used to assess the magnitude of the effect of mineral matter in the coal on the boron coating. The oxidative stability of the boron-modified carbons was determined from the decomposition curves obtained from the thermogravimetric analysis.

Modification of the as-received, KOH-treated carbon yielded oxidatively stable carbons up to an initial temperature of 520°C , compared to about 350°C for the starting material. Similar results were obtained for the carbonized Gascoyne lignite. Sulfurous acid washing of the Gascoyne significantly enhanced the thermal stability (600°C) of the boron-modified carbon.

INTRODUCTION

A major limitation in the use of carbons is their oxidative instability in air at high temperatures, usually greater than 400°C . At higher temperatures, the carbon reacts with oxygen in the air to produce CO and CO_2 . Some high-surface-area carbons could be utilized as catalysts or catalyst supports or in separation technologies at higher temperatures if they could be stabilized against oxidative degradation.

The application of a protective layer on the carbon surface could block oxygen from reacting with the surface carbons, or it could inhibit the reaction of oxygen with the surface carbon. Previous work demonstrated that boron atoms substituted for carbon atoms on the surface of a carbon fiber, composite, or graphite inhibits the oxidation reaction (1). Diffusion of boron via solid contact was attempted but gave low incorporation. Recently, a CVD reaction was used to form a protective layer on carbon fibers (2). This procedure resulted in a high concentration (25%) of boron, corresponding to the formula BC_3 . A similar reaction of boron trichloride and benzene vapors on a hot activated carbon surface could form a similar boron carbide protective coating. In this paper, we report the preparation and performance of the protective layer formed in this manner on sorbent and catalytic carbons.

EXPERIMENTAL

Preparation of CVD Carbons

As-received Coal Corporation of Victoria (CCV) lignite carbon was dried at 110°C overnight. The predried carbon (1.62 g) was packed in a quartz tube. The tube was placed in a vertical furnace and attached to a gas inlet. The outlet was attached to a bubbler filled with NaOH solution to trap HCl or BCl_3 . The carbon was heated to 727°C , and vapors of BCl_3 diluted with vapors of helium saturated with benzene were passed through the carbon. The CVD was carried out for 4 hours.

In some cases, benzene was not used, and vapors of BCl_3 diluted with nitrogen were used for carbide deposition.

The vapor-deposited carbon was annealed by heating in a gentle flow of helium at 900°C for 72 hours. The annealed carbon was grayish with a silvery mirror. The weight of the annealed carbon was 1.6 g.

TGA Determinations of Stability in Air at High Temperatures

Determinations of stability in air were conducted in a Dupont Thermal Analyst 2100 system with the TGA 951 analyzer module. Samples (50 mg) were heated at a rate of $25^\circ\text{C}/\text{min}$ in an air stream.

RESULTS

Boron-Deposition on KOH-Activated Carbon

Several carbons and chars were treated to increase their stability in air or hydrogen atmospheres. Initially, the chemically activated carbon produced by the KOH method was utilized. This carbon was prepared in Australia (CCV) from Gascoyne, North Dakota, lignite by pyrolysis in KOH. The CCV carbon had a high surface area (N_2 -BET = $1325 \text{ m}^2/\text{g}$) but was not as thermally stable as a carbon prepared by steam activation. The thermogravimetric analysis (TGA) tests in air showed that the CCV carbon began to react with air at 351°C (Table I), and at 660°C , the carbon was completely consumed. The decomposition curve was smooth, and the derivative peak was symmetrical, indicating a consistency in the oxidation mechanism. The residue present after the TGA experiment indicated an ash content of 7.3%. Much of the residue is potassium remaining from the earlier activation procedure. It is difficult to wash out all the potassium salts, and they can be the cause of the lower stability of the CCV lignite. The potassium salts will catalyze the gasification-combustion reactions that occur as the carbon is heated in air (or another reactive atmosphere).

Chemical vapor deposition was performed by passing a helium stream containing boron trichloride and benzene vapors through the CCV carbon at 727°C for 4 hours. The carbon was further treated by annealing at 900°C in the helium stream for 72 hours. The TGA test with the resulting carbon demonstrated an increased stability; the oxidation was not initiated until 507°C and was completed at 854°C . The decomposition curve was a little less symmetrical, indicating two different types of material or mechanisms were involved in the gasification-combustion reaction with air. In this experiment, an ash representing 11.2% of the material remained after the TGA experiment was completed. Thus a substantial amount of boron had been added.

A control experiment was performed by heating the CCV carbon in a helium stream with no reagent gases at 727°C , followed by annealing at 900°C . The TGA test on this sample exhibited an initial oxidation at 381°C , and the oxidation proceeded more slowly than the oxidation of the original CCV carbon, but this was higher than the oxidation rate of the CVD carbons. The ash content was 7.2%, similar to that of untreated CCV carbon. Thus the annealing procedure appeared to increase the stability by only a small factor, probably due to removal of the more reactive carbon material.

The presumed reaction is substitution of boron on the benzene or benzene decomposition products to form a graphitic layer with substitutional boron (2). It seemed possible that boron could form a protective coating on an activated carbon in the absence of the benzene by reacting directly with the carbon surface. Thus a second CVD experiment was performed with the CCV carbon, in which a helium stream containing only the boron trichloride was passed through the heated (727°C) carbon. The carbon was annealed as before. The TGA test of the carbon produced by this method showed an initial oxidation temperature of 518°C , but the decomposition occurred more rapidly, being complete at 777°C . In this case, the ash weight was 4.4%, indicating that some of the potassium present in the carbon must have been lost. The chlorine liberated from the boron trichloride may have formed potassium chloride which devolatilized at the high temperatures.

Boron Deposition on Gascoyne Char

Several reactions were performed with a Gascoyne carbon that was produced by carbonizing a cleaned lignite under conditions similar to those used in the CVD procedure. The lignite was washed with sulfurous acid to exchange out the calcium and alkali metals associated with the carboxylate groups of the coal. The exchanged coal was carbonized at 727°C and then 900°C to produce the carbon precursor for the CVD experiments. The control experiment on the carbon from the acid-exchanged Gascoyne gave an initial oxidation temperature of 527°C . The ash content of the untreated carbon was 5.8%.

A CVD carbon was then prepared from the 900°C -annealed carbon using a helium stream containing boron trichloride and benzene vapors at 727°C . The resulting carbon was annealed at 900°C . The TGA of this CVD carbon showed a remarkable improvement in stability, with an initial oxidation temperature of 600°C and complete oxidation at 890°C (See Figure 1). The ash content of this material was 12.85%, indicating a substantial amount of boron was incorporated.

Treatment of the 900°C -annealed carbon with boron trichloride vapor in helium (no benzene) was performed at 727°C for 4 hours, followed by annealing at 900°C to give the CVD carbon. The TGA test with this CVD carbon showed an initial oxidation temperature of 522°C , similar to that obtained from the 900°C -annealed precursor carbon. The ash content obtained in this test was 8.8%, indicating that boron was incorporated, even though benzene was not added to condense with the boron.

The addition of a carbon vapor source (benzene) to the boron trichloride generated an effective protective boron carbide coating on the surface of the lignite-derived carbons. The lower stability of the CVD carbons produced by boron trichloride vapor alone compared to the carbons produced by boron trichloride-benzene CVD carbon suggests that the carbon structures are different in these two types of samples, but we do not yet understand what boron forms are present. Although aromatic volatile compounds released during carbonization of a lignite might decompose to provide the carbon needed for the boron carbide layer, the type of volatile carbon species released in the gasification of an activated carbon at 727°C (CO, CO₂, CH₄) may react with the boron differently or not at all. On the other hand, condensation of the boron and carbon species generated from decomposition of the benzene and boron trichloride gases does form a protective edge structure or layer. Boron carbide has also been deposited on carbon fibers in a high-temperature (1200°-1500°C) reaction of boron trichloride vapor with hydrogen (3).

Carbonization of an as-received Gascoyne lignite was also studied to determine whether the mineral content of the resulting carbon affects the oxidation of the carbon. For the control (non-CVD), the lignite was first carbonized at 400°C, then 727°C, and finally 900°C. The initial oxidation temperature was similar to that obtained from similar thermal activation of the acid-washed lignite discussed above. When the char produced at 400°C was treated with boron trichloride vapor in helium for 2 hours at 727°C and then annealed at 900°C, the TGA test on this CVD carbon gave an initial oxidation temperature of 503°C. Thus, the stability actually decreased as a result of the boron treatment. The ash content of this boron-CVD carbon was quite high (16.0%). It is likely that much of the ash represents reactions of the mineral matter with the BCl₃ to form calcium and sodium chloride.

When the boron trichloride vapor treatment was continued for 4 hours, the resulting CVD carbon showed an initial oxidation temperature of 516°C and final burnout at 826°C. This is still somewhat less stable than the carbons produced without boron CVD.

CONCLUSIONS

The stability of activated carbons to air oxidation was remarkably improved by CVD with boron trichloride and benzene vapors. A boron carbide layer on a lignite-derived carbon was able to increase the stability to air oxidation so that the carbon could be used in an air stream at 600°C without decomposition. A very high surface area carbon was stabilized significantly by the CVD of boron carbide.

REFERENCES

1. Jones, L.E.; Thrower, P.A. *Carbon* **1991**, 29, 251.
2. Fecko, D.L.; Jones, L.E.; Thrower, P.A. *Carbon* **1993**, 31, 637.
3. Vincent, H.; Vincent, C.; Scharff, J.P.; Mourichoux, H.; Bouix, J. *Carbon* **1992**, 30, 495.

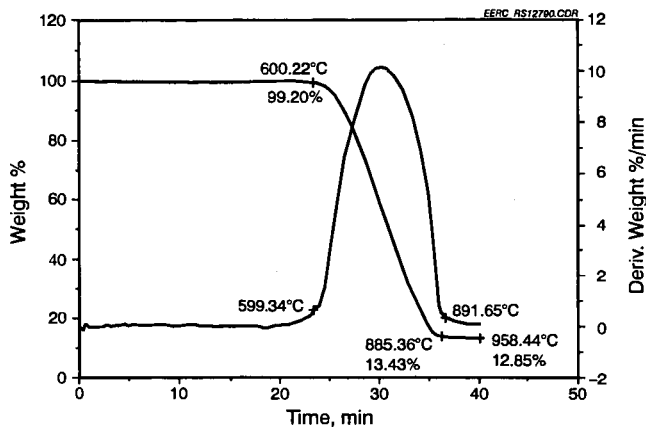


Figure 1. TGA of CVD-Gascoyne Activated Carbon

TABLE I

Chemical Vapor Deposition on Carbons			
Carbon/Char, g	CVD Method	Activation	Init. Oxid. Temp.
CCV-Lig	-	-	351
CCV-Lig	$\text{BCl}_3 + \text{He}/727^\circ\text{C}/4 \text{ hr}$	$900^\circ\text{C}/\text{He}/72 \text{ hr}$	519
CCV-Lig	$\text{BCl}_3 + \text{benzene} + \text{He}/727^\circ\text{C}/4 \text{ hr}$	$900^\circ\text{C}/\text{He}/72 \text{ hr}$	507
CCV-Lig	-	$727^\circ\text{C}/\text{He}/4 \text{ hr}$ $900^\circ\text{C}/\text{He}/72 \text{ hr}$	381
Gascoyne/carb. 400°C	$\text{BCl}_3 + \text{He}/727^\circ\text{C}/4 \text{ hr}$	$900^\circ\text{C}/\text{He}/72 \text{ hr}$	516
Gascoyne/carb. 400°C	$\text{BCl}_3 + \text{He}/727^\circ\text{C}/2 \text{ hr}$	$900^\circ\text{C}/\text{He}/72 \text{ hr}$	503
Gascoyne/carb. 400°C	-	$727^\circ\text{C}/\text{He}/4 \text{ hr}$ $900^\circ\text{C}/\text{He}/72 \text{ hr}$	532
Gascoyne/carb. $400^\circ\text{C}/727^\circ\text{C}/4 \text{ hr}/$ $900^\circ\text{C}/72 \text{ hr}$	$\text{BCl}_3 + \text{He}/727^\circ\text{C}/4 \text{ hr}$	$900^\circ\text{C}/\text{He}/72 \text{ hr}$	536
Gascoyne $\text{H}_2\text{SO}_3\text{-Cl}/\text{carb. } 400^\circ\text{C}$		$\text{He}/727^\circ\text{C}/4 \text{ hr}$ $900^\circ\text{C}/\text{He}/72 \text{ hr}$	527
Gascoyne $\text{H}_2\text{SO}_3\text{-Cl}/$ carb./4 hr/727°C/4 hr 900°C/72 hr	$\text{BCl}_3 + \text{He}/727^\circ\text{C}/4 \text{ hr}$	$900^\circ\text{C}/\text{He}/72 \text{ hr}$	522
Gascoyne $\text{H}_2\text{SO}_3\text{-Cl}$ carb./4 hr/727°C/4 hr 900°C/72 hr	$\text{BCl}_3 + \text{benzene} + \text{He}/727^\circ\text{C}/4 \text{ hr}$	$900^\circ\text{C}/\text{He}/72 \text{ hr}$	600

$\text{H}_2\text{SO}_3\text{-Cl} = \text{H}_2\text{SO}_3 - \text{Cleaned}$

QUANTITATIVE DETERMINATION OF THE FLUID AND INERT COMPONENTS DURING COAL CARBONISATION BY HIGH TEMPERATURE IN-SITU ^1H NMR

M. Mercedes Maroto-Valer, John M. Andréen and Colin E. Snape

University of Strathclyde, Department of Pure and Applied Chemistry, 295
Cathedral Street, Glasgow G1 1XL, Scotland, UK

Keywords: Thermoplasticity, inert material, high temperature ^1H NMR.

Although high temperature in-situ ^1H NMR has successfully been used previously to investigate the development of plasticity during coal carbonisation, the proportions of rigid and fluid material have rarely been determined. This has been achieved here using a high temperature Doty NMR probe operating at a frequency of 100 MHz. At maximum fluidity, the mobile phase accounts for up to 45% of the total hydrogen. Indeed, the fluid component increases both in terms of concentration and mobility up to maximum fluidity. Decreasing the particle size below 150 μm suppresses softening, but at maximum fluidity, the concentration of inert component is independent of the particle size.

INTRODUCTION

Although standard empirical tests such as Gieseler plastometer and Audibert-Arnu dilatometer are widely used to ascertain the plasticity behaviour of coking coals ⁽¹⁾, these tests do not easily relate to the actual structural changes that occur. High temperature in-situ ^1H NMR has successfully been used to investigate the motion of coals in-situ during carbonisation, where parameters reflecting the spin-spin relaxation times T_{2s} , have been correlated with plasticity ⁽²⁾. There are usually two contributions to the ^1H NMR signals of coals: a mobile component with a Lorentzian decay, and an inert component with a Gaussian distribution ⁽³⁾. Coal being a macromolecular network contains a substantial inert component which does not soften and forms the broad constituent of the NMR signal.

In the late 70's, Sanada and coworkers conducted the first high temperature ^1H NMR study on coal and pitches at the early stages of carbonisation ⁽⁴⁾. The development of plasticity in coals was monitored by changes in the half width of the spectra. However, due to experimental factors including the relatively small sample size and low magnetic field used (37.5 MHz for ^1H), the spectra could not be deconvoluted to derive the proportion of inert material present. This limitation was overcome from 1983 onwards by Lynch et al ^(2,3,5,6), who have referred to the technique as "Proton Magnetic Resonance Thermal Analysis" (PMRTA). They have used mainly the empirical parameter, M_{216} , corresponding to the spectrum truncated at 16 kHz which was found to be the optimum frequency for gauging changes in fluidity ⁽⁶⁾. However, in-situ ^1H NMR has not been used widely to determine the overall concentrations of fluid and inert material during coal carbonisation, due to the possibility of truncating broad Gaussian signals when signal to noise levels tend to be low at high temperatures. This has been achieved here using a high temperature Doty NMR probe operating at a frequency of 100 MHz. Three Australian bituminous coals with different plastic properties have been investigated and both the concentration and mobility of the fluid components have been monitored. Furthermore, for one of the coals investigated the effect of the particle size has been studied for fractions below 212 μm .

EXPERIMENTAL

Table 1 lists the proximate and maceral analysis as well as the Gieseler plastometer results for the three coals investigated. The coals were ground to $<212\ \mu\text{m}$. Sample AUS-1 was also ground to give <45 and $212\text{--}45\ \mu\text{m}$ fractions.

In the high temperature measurements, the 90° pulse width varied with temperature between $2.2\ \mu\text{s}$ at ambient to $3.0\ \mu\text{s}$ at 600°C . The solid echo pulse sequence ($90^\circ - \tau - 90^\circ$) with a refocusing of $5\ \mu\text{s}$ was used in order to minimise the loss of signal due to the dead time of the NMR coil. About $40\text{--}70\ \text{mg}$ of sample was packed in a zirconia container which was placed horizontally in the stator. A flow of $12\ \text{dm}^3\ \text{min}^{-1}$ of dry nitrogen was used to transfer heat to the samples and to remove the volatiles escaping through a small ventilation hole in the container. Spectra were obtained at a number of different temperatures and the free induction decays (FIDs) were transferred from the spectrometer to a PC for processing and fitted to Lorentzian and Gaussian components, as appropriate. The spectra obtained in the fluidity range could best be fitted to either one Gaussian and one Lorentzian component or two Gaussian components.

RESULTS AND DISCUSSION

General aspects Figure 1 shows the ^1H NMR spectra for sample AUS-1 obtained at 25°C , 453°C - maximum fluidity and 529°C - after resolidification. Figure 2 compares the peak widths at half height, $\Delta H_{1/2}$, measured in-situ at temperatures up to 600°C for the three coals and Figure 3 shows the deconvoluted spectra for two of the coals at the temperature of maximum fluidity. The coals behave in a similar way with a constant $\Delta H_{1/2}$ corresponding to single Gaussian component before the onset of thermoplasticity ($300\text{--}350^\circ\text{C}$). The maximum fluidity at $430\text{--}480^\circ\text{C}$ is reflected by the minimum in $\Delta H_{1/2}$, corresponding to a maximum in T_2 . During the fluidity range, the peak width of the plastic phase is only between 20 and 30% of that for the initial coal. Comparable observations in peak half width have been reported earlier by Sanada (4,7) and by Lynch et al. Using the M_{2T16} parameter (5,6). As expected, the fluid component has its highest contribution to the total NMR signal at maximum fluidity.

After the onset of resolidification, ($470\text{--}510^\circ\text{C}$) the average peak width increases to reach a value similar to that of the initial coal with only a single Gaussian component being observed. The inert component represented by a Gaussian distribution has a relatively constant T_2 of $\approx 20\ \mu\text{s}$ throughout the temperature range studied (Table 2).

Proportions of rigid and fluid material For the coals investigated, Table 2 lists the proportions of these components at maximum fluidity and their associated spin-spin relaxation times (T_2 s). The data ($<212\ \mu$ fractions indicate that the extent of fluidity development for AUS-4 is much less than for AUS-1 and AUS-8 (Table 2). It generates a lower concentration of fluid material that has considerably less mobility than that for the other coals (Table 2). Indeed, the spectrum at maximum fluidity for AUS-4 can be fitted using only two Gaussian components, without including the Lorentzian for the most fluid material. Further, Figure 2 indicates that maximum fluidity is attained at a lower temperature for AUS-1 and AUS-8 than AUS-4, consistent with the Gieseler plastometer data. For AUS-8, the concentration of inert material only accounts for 56% of the total hydrogen observed (Table 2).

Figure 4 shows the evolution of the fluid component for sample AUS-1. During the plastic stage, the T_2 or mobility of the Lorentzian component increases, together with its contribution to the total signal. This reaches a maximum at 450°C and then decreases during the resolidification process. Thus, the

development of fluidity and subsequent resolidification in the coals follow the same trend involving changes in both concentration and mobility of the plastic phase.

Particle size For AUS-1, the particle size has a significant effect on the development of fluidity. Table 3 lists the proportions of rigid and mobile material and their T_{2s} at maximum fluidity for the three different particle size fractions studied. The mobility of the narrowest component is suppressed for the $<45\mu\text{m}$ fraction, and there is still a noticeable difference between the <212 and $212-45\mu\text{m}$ fractions. The suppression of fluidity with decreasing particle size is represented by a reduction in the mobility of the fluid material, rather than a reduction in its concentration. This reduction in fluidity may be ascribed to either an oxidation effect or a combination of reduced voidage between the coal particles and the fact that fluid material will escape easier from smaller particles. Careful grinding of the coal and high temperature NMR analysis of the resultant fractions strongly suggests that the latter is the prime cause of the fluidity loss. Furthermore, it has been shown that fluidity is essentially a reversible phenomenon provided that the sample is cooled rapidly from the temperature of maximum fluidity.

CONCLUSIONS

The results have confirmed the ability of high temperature ^1H NMR to follow coal carbonisation in-situ. The approach used here is able to describe the carbonisation process in terms of the proportions of rigid and fluid material as well as the mobility of the latter. Decreasing the particle size below $150\mu\text{m}$ suppresses softening, but at maximum fluidity, the proportion of inert material is independent of the particle size.

ACKNOWLEDGEMENTS

The authors thank the European Coal & Steel Community (Contract Nos.: 7220-EC/870 and 7220-EB/845) and the Basque Government (studentship for M.M. Maroto-Valer) for financial support.

LITERATURE CITED

1. D.W. van Krevelen, Coal, 3rd Revised Edn, Elsevier, Amsterdam, 1993, Chs.23- 24.
2. L.J. Lynch, D.S. Webster, R. Sakurovs, W.A. Barton and T.P. Maher, Fuel, 1988, **67**, 579.
3. T.J. Parks, L.F. Cross and L.J. Lynch, Carbon, 1991, **7**, 921.
4. K. Miyazawa, T. Yokono and Y. Sanada, Carbon, 1979, **17**, 223.
5. L.J. Lynch and D.S. Webster, American Chemical Society Symposium Series, 1983, **230**, 353.
6. R. Sakurovs, L.J. Lynch and W.A. Barton, Amer. Chem. Soc. Adv.in Chem. Series, 1993, **229**, 229.
7. T. Yokono, T. Obara, Y. Sanada and K. Miyazawa, Carbon, 1984, **2**, 169.

Table 1 Proximate analysis, vitrinite reflectance, atomic H/C and temperature of maximum fluidity determined by Gieseler and NMR for the coals investigated.

	VM (db)	Ro (max)	atomic H/C	Tem. max / °C
AUS-1	23.1	1.20	0.60	451 (453) ^a
AUS-4	19.63	1.46	0.61	472 (470)
AUS-8	33.94	0.86	0.74	460 (460)

^a Values in brackets were determined by ¹H NMR.

Table 2 Deconvolution into two components identified in the ¹H NMR spectra obtained at maximum fluidity for the three coals investigated.

	% rigid	T ₂ rigid / μs	% mobile	T ₂ mobile / μs
AUS-1*	62	20.7	38	82
AUS-4**	81	20.9	19	68
AUS-8*	56	22.2	44	92

* Deconvoluted into one Gaussian and one Lorentzian components.

** Deconvoluted into two Gaussian components.

Table 3 Deconvolution into two components of the ¹H NMR spectra obtained at maximum fluidity for AUS-1 as a function of the particle size.

	%rigid	T ₂ rigid / μs	% mobile	T ₂ mobile / μs
<45μm	63	18.5	37	48
<212μm	62	20.7	38	82
45μm - 212μm	68	23.3	32	111

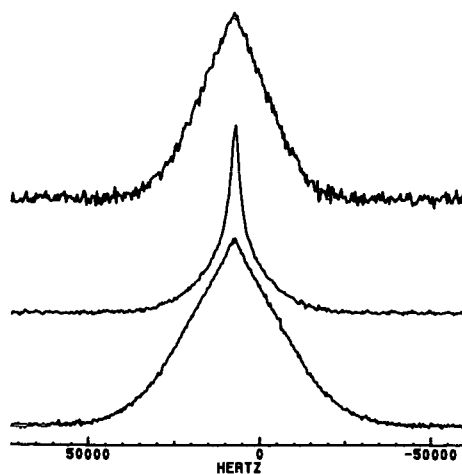


Figure 1 ¹H NMR spectra for AUS-1 at 25°C (bottom), maximum fluidity at 453°C (middle), and resolidification at 529°C (top).

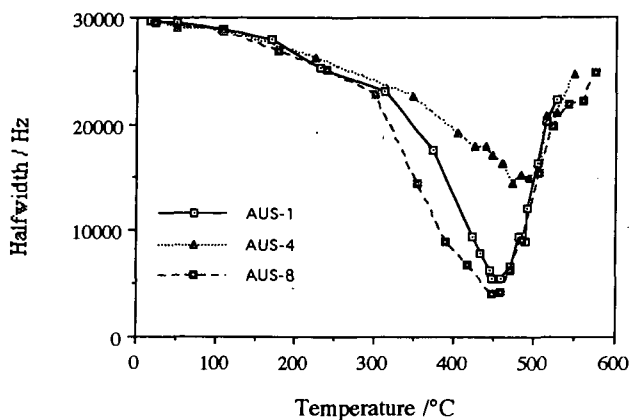


Figure 2 Variation in the average peak half-width for the three coals investigated ($<212 \mu\text{m}$). The peak half-width is dominated by the contribution from the mobile component close to maximum fluidity.

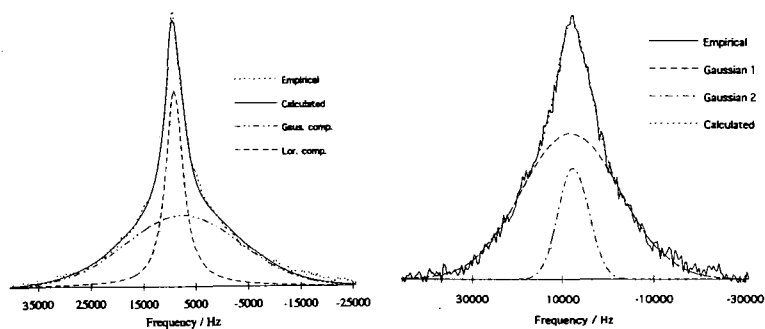


Figure 3 Deconvoluted ^1H NMR spectra at maximum fluidity for AUS-1 (right), and AUS-4 (left).

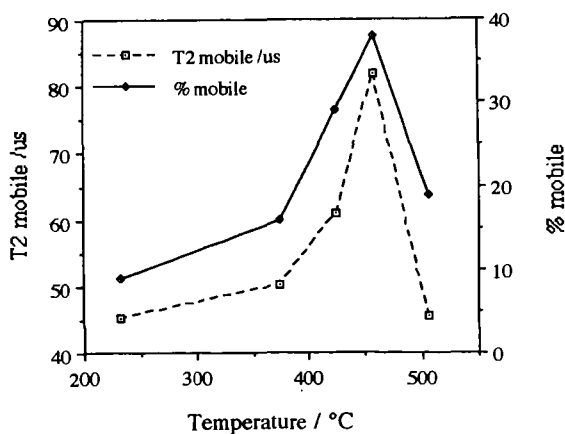


Figure 4 Evolution of the fluid component for AUS-1 with temperature.

EVAPORATIVE LIGHT SCATTERING DETECTION IN QUANTITATIVE HPLC OF PAC MIXTURES AND COAL-TAR PITCHES

Vicente L. Cebolla, Luis Membrado, Jesús Vela, Ana C. Ferrando, and Clemente Romero
Departamento de Procesos Químicos
Instituto de Carboquímica, CSIC
P.O. Box 589, 50080 Zaragoza, Spain

Keywords: evaporative light scattering detector, HPLC, polycyclic aromatic compounds

INTRODUCTION

The term Polycyclic Aromatic Compounds (PACs) include a wide variety of classes of compounds. In turn, the number of possible PACs for each class is of astronomical proportion (1, 2). Environmental and fossil-fuel samples are composed of very complex mixtures of unknown PACs. The strategy for their analysis depends, among others, on the nature of matrix and PAC concentration, and involves cleanup/prefractionation steps and HPLC analysis. Therefore, HPLC detectors must be calibrated with pure reference standards for every substance to be quantified. However, only a relatively small fraction of PACs can unambiguously be identified and are commercially available (2). An ideal detector for chromatography of complex mixtures should provide uniform response factors for each separated compound or class of compounds. None of the conventional HPLC detectors (UV, Refractive Index, fluorescence) meet this requirement, neither for mixtures of unknown but well-separated pure peaks nor for compound-class fractionation of fossil fuels (where other additional problems can occur, such as presence of very heavy and polar PACs, quenching problems using fluorescence detection, need of tedious absolute calibrations, etc.)

It has been reported that the Evaporative Light Scattering Detector (ELSD) enables all types of non-volatile solutes to be detected (3, 4), although it has recently been reported that solutes having a lower volatility than the mobile phase can be analyzed working at mild temperatures (5). Detector response has been reported to be quite independent of the chemical composition of the solute. However, very different response factors were reported in the past in the case of semi-volatile PACs (6). This work intends: i) to evaluate the possibility of the application of ELSD in order to quantify PACs in complex mixtures, ii) to theoretically justify the responses of the studied PACs, and iii) to lay the groundwork for application to fossil-fuel characterization.

EXPERIMENTAL

The HPLC system consisted of: a Waters 510 pump, a 7725i Rheodyne injector, a PL-Gel Mixed-E (30 cm length, 3 μ m particle size with mixed pore distribution), and a PL-EMD 950 ELSD. GPC-grade-Tetrahydrofuran (THF) stabilized with BHT was used as mobile phase. Flow rate was 1 ml/min. The output signal from the detector was fed into a Fluke Hydra 2620 multichannel data acquisition unit, and stored in an HP 100LX computer for data acquisition. Raw data were further reprocessed using an adequate spreadsheet in a 486 PC clone.

The operating mode of ELSD is as follows: the effluent from the chromatographic column enters a Venturi nebulizer and is converted into an aerosol by a stream of air (12 l min⁻¹). Venturi consists of a stainless steel capillary tube (0.25 mm i.d., 1.59 mm o.d.) carrying the column effluent, which is surrounded by a larger tube (2 mm i.d.). The fine droplets formed are then carried out through a temperature controlled drift tube which causes evaporation of the mobile phase to form small particles of non-volatile solute. This cloud of solute passes through a white light in the broad-band 400-700 nm, which produces light scattering, which in turn is detected by a photomultiplier at a 60° angle. The evaporation temperature used was 30°C.

The amounts (μ g) of the studied PACs reported throughout the text correspond to the mass effectively injected. The response factor of each standard is defined as its corresponding area, A (counts as μ V s⁻¹) per mass unit, m (μ g). Only absolute response factors are used throughout this paper.

RESULTS AND DISCUSSION

Quantification of PACs using ELSD

In a first step of the research, detector response (A) vs sample load (m) was evaluated for pure PACs, and binary mixtures of PACs. In each mixture injected, either coronene or 2-hydroxycarbazole was used as reference standard due to their adequate retention time using the above-mentioned column. Although adequate regression coefficients ($r = 0.999$) were obtained for the studied PACs using linear regressions, deviations from the theoretical linearity at low sample loads were evidenced by: i) significantly lower response factors for each pure PAC as sample load decreased (Table 1), ii) in the case of mixtures, greater differences between area percentages from the chromatogram and known mass percentages (hereafter referred as to A - m differences) at low sample loads (Table 1), and iii) a better fit of experimental data to logarithmic regressions ($\log A = \log a + b \cdot \log m$, from $A = a \cdot m^b$). Parameters from both types of regression for some different PACs are given in Table 2. Values of a and b are similar for the studied PACs despite their different chemical nature, suggesting similar responses. The physical meaning of b , and the agreement between the experimentally obtained and

theoretically calculated b values for the studied PACs are explained later in this work, as well as a theoretical justification of linearity deviation. This is inherent to ELSD regardless of the volatility/involatility of the PACs. Recent results reported by Dreux et al. (5) showed a similar behavior in the case of glucose analysis on an octadecyl bonded silica when using either ELSD or Refractive Index detector. They demonstrated that linearity deviation is even larger in the latter case. The sample load range in which ELSD behaves in a non-linear fashion depends on the considered PAC (Table 1, results at 20 and 40 μg). Results from Table 1 at 40 μg (in the linear zone of ELSD) show that the studied 3-6 ringed, semi-volatile polycyclic aromatic hydrocarbons (PAHs) can be analyzed using ELSD under the described mild conditions with A-m differences lower than 6 % w/w. The same can be said for other analyzed hydroxy-PAHs, and heteronuclear PACs. All these standards presented quite uniform response factors despite their different chemical natures. Therefore, ELSD can be used in this zone *for the analysis of complex mixtures of PACs in which there are unknown components, avoiding any calibration step*. This is an advantage with regard to the other conventional HPLC detectors, such as UV, Refractive Index and fluorescence. At low sample loads, ELSD needs a calibration step and can be useful for mixtures of known PACs, in the same manner than the other HPLC detectors. From the point of view of quantitative accuracy, b does not have to be equal or close to unity providing an accurate value is known (7).

Are low-sized PACs really underestimated using ELSD?

The chromatographic quantification of PACs and other related compounds (with b.p. and MW lower than 285°C and 300 u.m.a., respectively) using ELSD was questioned in the past (6, 8). However, our results show reasonably uniform response factors in the linear zone of ELSD in the case of PACs with these characteristics. A partial volatilization of all the studied PACs due to the nebulization and evaporation must be discarded, given the negligible volatility, for instance, of coronene ($P_0 = 1.63 \times 10^{-3}$ mm Hg at 150°C) at the mild conditions used (30°C). Semi-volatile PAHs with 3-6 aromatic rings, small-sized N-heteronuclear PACs and hydroxy-PAHs present similar response factors to hardly volatile coronene, and therefore can be analyzed using mild working conditions.

The impossibility of analyzing PACs using ELSD was exclusively attributed to the supposed volatility of these compounds. Although this should not be discarded in some cases, results presented here suggest that the values of the corresponding response factors reported in the literature were estimated at low loads and/or higher temperatures than those used here. As well, there have been changes in the configuration of nebulizers in the newer models with respect to the older ones. Nebulization directly influences particle diameter, which in turn affects the sensitivity of ELSD for different solutes, as explained in the last section of this work.

It must be stressed that the volatility of a given compound cannot merely be predicted from its b.p. and MW (3). For instance, although acenaphthene and 2-naphthol have similar b.p. and MW, the former showed no signal from ELSD under the conditions used, while the latter gave a high response factor. Vapor pressure at a given temperature (if possible) is a better parameter to compare relative volatilities although it should be taken with caution because ELSD evaporates in an air flow.

However, there is a value of vapor pressure for a given temperature over which PACs cannot be analyzed using ELSD. Thus, two-ring PACs (naphthalene, 2-methylnaphthalene), and low-sized, non-planar, hydrogenated PACs (acenaphthene, fluorene), showed either no signal or an important loss of response at 30°C, as expected given their high vapor pressures.

Agreement between theoretical and experimental data on evaporative light scattering response of PACs. Why are response factors of studied PACs reasonably uniform under the used working conditions?

The stages involved in evaporative light scattering detection are: nebulization of the HPLC effluent, evaporation of the mobile-phase droplet cloud, and scattering of incident light.

Nebulization depends on the mobile phase properties and flow rate, nebulizer geometry and nebulization conditions, through Mugele and Evans' droplet size distribution (9), and the equation of Nukiyama and Tanasawa, as reported by Van der Meeren et al. (10). Details of all calculations presented here are reported elsewhere (11). The droplet size distribution (in volume) under our working conditions is given in Figure 1.

After evaporating, the diameter of solute particles (d) can be related to the concentration, C , through

$$d_i = d_m (C / \rho_i)^{1/3}$$

where ρ_i is the solute density, and d is each value of the droplet diameter distribution after nebulization. C is function of both time and chromatographic conditions according to

$$C = \frac{X/10^9}{Q_i} \frac{\exp [-(t_r - t)^2 / (2sd^2)]}{(2\pi)^{1/2}sd}$$

where X is the sample load, Q , is the mobile phase flow rate and sd and t , are the standard deviation and retention time of the chromatographic peak, respectively. This means that each point of a given chromatogram has its corresponding particle size distribution. The highest diameters in the distributions correspond to the maximum of each peak. Figure 2 shows nine size distributions corresponding to the first half of the chrysene peak. Figure 3 gives the particle size distributions at peak maxima in the cases of chrysene and coronene. Particle size distributions for the studied PACs are similar because their densities are not very different (between 1100 and 1300 kg m⁻³, approximately).

ELSD is a detector which presents different sensitivities with regard to the scattering domain of work (Rayleigh, Mie, reflexion-refraction). These domains are determined by the ratio of a characteristic dimension (e.g. diameter, d) of the solute particle to the wavelength(s) of the incident light beam (λ) (12). It is very important to work in similar d/λ ranges in order to have homogeneous response factors for the components of a complex mixture. Rayleigh scattering is predominant when d/λ is smaller than 0.1. In this domain, the intensity (I) of scattering increases very rapidly with increasing particle diameter (d). I is lower for particles in the Rayleigh domain than for other domains. Mie scattering becomes preponderant when d/λ is greater than 0.1. In this domain, I increases as the fourth power of diameter. For greater d/λ ratios (approximately 2), reflexion and refraction become dominant and sensitivity increases. (I is function of diameter squared). I from spherical particles can be calculated for any size using Mie's theory. Therefore, when I is expressed in function of the concentration, (13) through particle diameter ($d = d^* (C/\rho)^{1/3}$), then $I = f(C^2)$, $f(C^{1/3})$ or $f(C^{2/3})$, for Rayleigh, Mie or reflexion-refraction domains, respectively. In Table 2 it can be seen that experimentally obtained b values for PACs are between 1.29 and 1.47, that is, near to the theoretical value for Mie's domain. Calculations of d/λ from particle size distributions are in agreement with this. The highest d/λ for chrysene (at 40 μ g, at the maximum of the peak, and for $\lambda=400$ nm) is 1.05. The homogeneous response of PACs is illustrated by the similar values of d/λ for chrysene and coronene (Figure 3).

Application of ELSD to HPLC-compound class fractionation and HPLC-GPC of fossil fuels

Besides the above-mentioned quantitative application of ELSD for analyzing mixtures of unknown PACs, this detector presents several advantages with respect to Refractive index detector, in the case of compound-class fractionation of fossil fuels, in general: possibility of using gradients of eluants and typical eluants of reversed phase, rapid stabilization with temperature, and adequate baseline (no negative peaks, no solvent fronting). More particularly, coal-tar pitches mainly consist of PAHs and their heteronuclear analogues (14). Therefore, the PACs studied in this work represent quite well a part of PACs found in coal-tar pitches. These are usually analyzed using HPLC-compound class characterization after a chromatographic prefractionation. According to our results, ELSD could be used to quantify this type of analysis. GPC-ELSD has been carried out to obtain comparative curves of size distribution for coal-tar pitches, using the same column as that used here (15). Given that no discrete peaks are obtained with this technique, more research is needed to understand the influence of nebulization and chromatographic conditions on particle diameter in order to perform semi or quantitative analyses.

ACKNOWLEDGEMENTS

The authors are grateful to Spanish DGICYT (Project PB93-0100) and ECSC (European Steel & Coal Community, Project 7220-EC/765) for their financial support

REFERENCES

1. Vo-Dinh, T. In "Chemical Analysis of Polycyclic Aromatic Compounds", ed. by Vo-Dinh, T. Chemical Analysis, vol. 101, John Wiley & Sons, New York, 1989, ch. 1.
2. Lafleur, A.L.; Monchamp, P.A.; Plummer, E.F.; Wornat, M.J. *Anal. Letters* **1987**, *20*, 1171.
3. Charlesworth, J.M. *Anal. Chem.* **1978**, *50*, 1414.
4. Lafosse, M.; Elfakir, C.; Morin-Allory, L.; Dreux, M. *J. High Resol. Chromatogr.* **1992**, *15*, 312.
5. Dreux, M.; Lafosse, M.; Morin-Allory, L. *LC-GC International* **1996**, march.
6. Coulombe, S. *J. Chromatogr. Sci.* **1988**, *26*, 1.
7. Scott, R.P.W. in "Quantitative Analysis using Chromatographic Techniques", ed. By Katz, E. Separation Science Series. John Wiley & Sons, New York, 1987, ch. 1, p. 24.
8. Bartle, K.D.; Taylor, N.; Mulligan, M.J.; Mills, D.G.; Gibson, C. *Fuel* **1983**, *62*, 1181.
9. Mourey, T.H.; Oppenheimer, L.E. *Anal. Chem.* **1984**, *56*, 2427.
10. Van der Meeren, P.; Vanderdeelen, J.; Baert, L. *Anal. Chem.* **1992**, *64*, 1056.
11. Cebolla, V.L.; Membrado, L.; Vela, J.; Ferrando, A.C., submitted to *J. Chromatogr. Sci.*
12. Kerker, M. "The scattering of light and other electromagnetic radiation", 2nd ed. Academic Press, Inc., New York, 1969.
13. Dreux, M.; Lafosse, M. *Analisis* **1992**, *20*, 587.
14. Alula, M.; Diack, M.; Gruber, R.; Kirsch, G.; Wilhelm, J.C.; Cagniant, D. *Fuel* **1989**, *68*, 1330.
15. Johnson, B.R.; Bartle, K.D.; Herod, A.A.; Kandiyoti, R. *Preprints Am. Chem. Soc., Div. Fuel Chem.* **1995**, *40* (3), 457.

Table 1. Response factors (A/m), and differences between area and mass percentages (Δ) of PAC standards in binary mixtures at several sample loads using either 2-hydroxycarbazole (HCBZ) or coronene (CRN) as references¹.

Standards	40 μg		20 μg		8 μg
	Δ^2	A/m	Δ^2	A/m	A/m
7,8-benzoquinoline	0.8	1.188	15.7	0.475	0.213
diphenyldisulfide	1.0	1.187 [‡]	7.0	0.621 [‡]	0.347
coronene	1.5	1.308	8.2	0.870	0.321
perylene	1.5	1.383	7.2	0.754	0.410
2-hydroxycarbazole	1.5	1.390 [‡]	8.2	1.220 [‡]	0.565
Benzo[a]pyrene	2.5	1.407	5.2	0.794	0.435
tianthrene	2.5	1.291	1.3	0.974	0.446
anthracene	2.6	1.002	7.0	0.733	0.536
acridine	2.6	1.523	4.7	1.138	0.319
phenoxazine	3.4	1.584 [‡]	10.1	0.994 [‡]	0.562
2-naphthol	4.2	1.301 [‡]	3.4	0.782 [‡]	0.243
9-phenanthrol	4.4	1.090 [‡]	1.7	1.166 [‡]	0.573
pyrene	4.7	1.478	5.1	1.147	0.563
fluoranthene	5.8	1.436	6.5	0.941	0.390
2,3-benzofluorene	6.1	0.850	8.3	0.638	0.320
9-hydroxyfluorene	6.7	1.454 [‡]	5.8	1.083 [‡]	0.550
carbazole	8.7	0.917 [‡]	7.6	0.634 [‡]	0.389
chrysene	9.7	0.857	9.2	0.647	0.345
phenanthrene	9.0	0.775	22.2	0.419	0.225

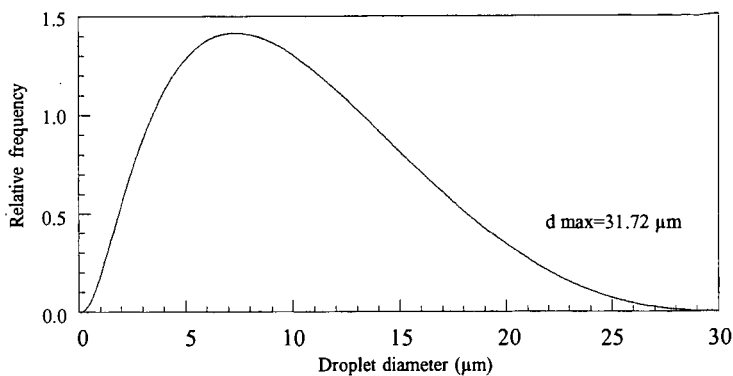
² Absolute value. [‡] Superscript ‡ indicates that coronene was the reference; the remaining refer to HCBZ.

Table 2.- Fitting of ELSD response vs sample load for three studied PACs.

	2-hydroxycarbazole	coronene	chrysene
Linear regression			
slope	1.542	1.537	0.994
intercept	-6.887	-10.07	-3.66
r	0.9995	0.9923	0.999
error % ¹ at 5 μg	17.0 ²	140.2	74.9
Logarithmic regression			
b	1.291	1.474	1.344
a	-0.340	-06677	-0.5897
r	0.9984	0.9999	0.9963
error % ¹ at 5 μg	-2.9 ²	0.04	-10.5

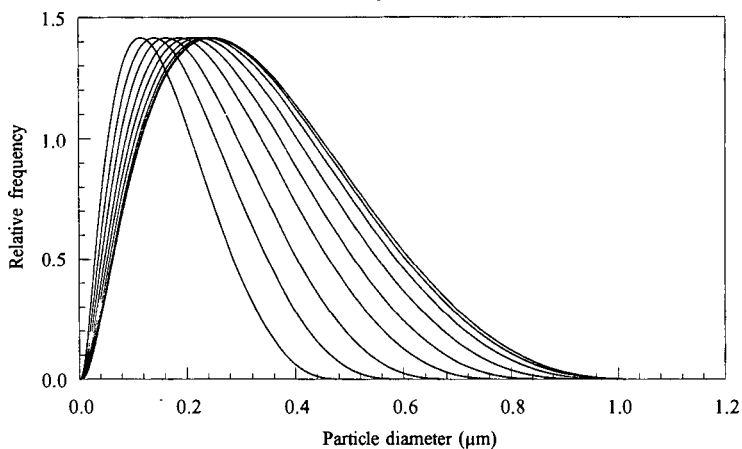
¹ Error % between the corresponding experimental value and that predicted from the corresponding fitting curve. ² In these cases, error % at 8 μg .

Figure 1



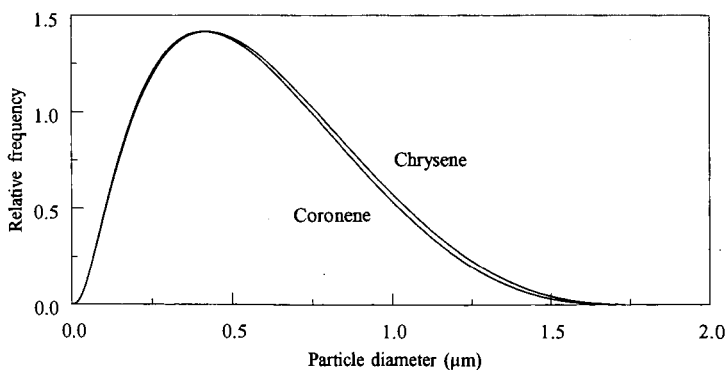
Droplet size distribution (in volume) from the nebulization of THF in a venturi.

Figure 2



Nine particle size distributions (in volume) corresponding to chrysene elution (5 μg load) from $t = t_r - w/2$ (start of peak) to $t = t_r$ (peak maximum)

Figure 3



Particle size distributions at peak maxima (40 μg) for chrysene and coronene

ANALYSES OF PRODUCTS FROM AUTOCLAVE REACTIONS: DERIVATION OF REACTION PARAMETERS

Belma Demirel

Center for Applied Energy Research

3572 Iron Works Pike, Lexington, KY 40511-8433, USA

and

Jan Paul

Bilkent University, Chemistry

Bilkent 06533, Ankara, Turkey

Keywords: Hydrocracking, Decalins, Faujasites

ABSTRACT

This work presents energetics for high pressure hydroprocessing reactions derived from post analyses of liquid and gaseous products. Specifically, GC and GC/MS were used to follow the product distribution from the hydrocracking of methyldecalins over zeolite supported palladium and platinum catalysts as a function of temperature. Plain Arrhenius plots summarize key results and reveal possible connections in terms of 'activation energies' between hydrogen consumption and the amounts of different products. The total cycloalkane production and the consumption of hydrogen both show a simple temperature dependence with the same 'activation' energies. Methane production varies more rapidly with temperature but can still be described by a single exponential term. The final example, conversion to aromatics, displays a more complicated dependence with an accelerated yield at high temperature. This form of data analyses connects to a new routine for mass balance evaluations and it is now applied to model catalyst performance and to understand optimum reaction conditions. Other branches of this project include surface spectroscopic measurements of fresh, sulfided and used catalysts, characterization of partially hydrogenated naphthalenes and modeling of hydrogen activity at metal sulfides.

INTRODUCTION

The present work is twofold motivated. The overall project goal is to find optimum conditions for a two-stage conversion of polyaromatic feeds, modelled by 1-methylnaphthalene (1-MeNapht), to fuels [1]. The first step, hydrogenation to methyldecalins (MeDecs) is addressed elsewhere [2]. Within the above engineering framework several scientific challenges constitute a second motivation. One challenge is to improve mass-balance evaluations [3], another to identify surface intermediates by a combination of spectroscopic tools and quantum chemical calculations [4], and yet a third to derive energetics from product analyses. The present work addresses the third topic.

Conversion, product distribution and potential for commercialization were recently demonstrated for an optimized two-stage operation with an initial hydrogenation stage of 1-MeNapht to MeDecs over $\text{NiMo/TiO}_2\text{-Al}_2\text{O}_3$ and a second hydrocracking stage of MeDecs over Pd/Faujasite [5]. This work was extended with weight change measurements and physico-chemical characterization of surface sulfides formed by pretreatment in $\text{H}_2\text{S/H}_2$ and of carbonaceous residues formed during operation [6,7]. The extension represents an additional improvement over previous schemes for mass-balance evaluations based solely on analyses of liquid and gaseous phases.

MATERIALS AND METHODS

The catalysts were either prepared with surface impregnation techniques from aqueous solutions followed by calcination in air and sulfidation in $\text{H}_2\text{S/H}_2$ (400°C, 2h) or, for ion exchanged Faujasites, used as received from the manufacturer [5]. 1-MeNapht (98%, Aldrich) was used as received for the first reaction stage. The feed for the second stage, MeDecs, was synthesized with better than 95% selectivity [2]. The catalysts and feed were mixed (1:4 to 1:10) in a stirred batch autoclave, operated either as a closed or an open system under hydrogen (700-1500 psi). The liquid product was weighed and analyzed by GC/MS. The composition of the gaseous product was analyzed by GC. The mass of hydrocarbon gases was derived from the pressure change (closed systems) or from the volume of the gas product. The hydrogen amount was calculated from the pressure change before and after reaction (closed systems) or from the change in H:C ratio from feed to product (closed and open systems).

RESULTS AND DISCUSSION

The prime result is a novel compilation of performance data for a series of two-stage reactions of 1-methylnaphthalene conversion to gasoline components using different catalysts. These data clearly show the conversion and potential for an industrial process and the ratio between gaseous and liquid products [1,5].

The scientific results are exemplified by two figures showing the evolution of products as a function of temperature over Pt (Fig.1) and Pd (Fig.2) ion-exchanged Faujasites.

Figs.1 shows that the hydrogen consumption and the total production of cycloalkanes over Pt/Faujasite are well described by a single Arrhenius term with the same apparent activation energy, 30 kJ/mol. Methane production is again well described by a single exponential term but with a considerably larger 'activation energy' 150 kJ/mol. The conversion to aromatics displays a more complicated volcano shape vs. temperature and it is not meaningful to derive a single slope over the entire temperature range.

Hydrocracking of MeDecs over Pd/Faujasite (Fig.2) shows a similar behavior with the following 'activation energies': hydrogen consumption 29 kJ/mol, total cycloalkane production 27 kJ/mol and methane production 130 kJ/mol. Aromatics production again shows a more complex temperature dependence.

The simple temperature dependence of hydrogen consumption and cycloalkane production motivates the search for a simple reaction mechanism involving both functionalities. The apparent 'activation energy' is too low to be translated directly to a certain bond activation process and its origin from possibly counteracting enthalpy and entropy terms is not clear.

The mechanism is different for methane production with an 'activation energy' of 130-150 kJ/mol. This branch of hydrocracking resembles the hydrogenation of surface carbon in Fisher-Tropsch catalysis.

The separate temperature dependence of the aromatics production shows that these compounds are formed neither along the same route as methane nor the cycloalkanes. A bell curve is often the result of competing processes, in our case the onset of dehydrogenation and/or cleavage reactions.

CONCLUSIONS

Quantitative analyses of liquid products and off-gases from autoclave studies of hydrocracking of methyldecals over Pd/Faujasite and Pt/Faujasite catalysts are presented. The data shows that the mechanism for cycloalkane production is closely related to the hydrogen activity i.e. most likely to the generation of adsorbed atomic hydrogen. It also shows that the route for methane production is separate from this mechanism as well as from the path leading to aromatic compounds.

ACKNOWLEDGEMENTS

We acknowledge collaborations with P.Nordlander at Rice and D.W.Goodman at Texas A&M within the framework of this project. B.Demirel would also like to express her sincere gratefulness to W.D.Wiser, Univ.of Utah, for his help and kindness during most of this project.

REFERENCES

1. Demirel B. and Wiser W.H., Hydrotreatment and Hydrocracking of Oil Fractions Oostende, Belgium, 1997, submitted
2. Demirel B. and Wiser W.H., ASC, Orlando, 1996
3. Demirel B. and Paul J., 7th NSC, Turku, 1996
4. Demirel B., Şafak S., Süzer Ş., Paul J., in progress
5. Demirel B., PhD Thesis, Univ.of Utah, 1996
6. Demirel B. and Paul J., MRS, Boston, 1996, submitted
7. Demirel B. and Paul J., Hydrotreatment and Hydrocracking of Oil Fractions Oostende, Belgium, 1997, submitted

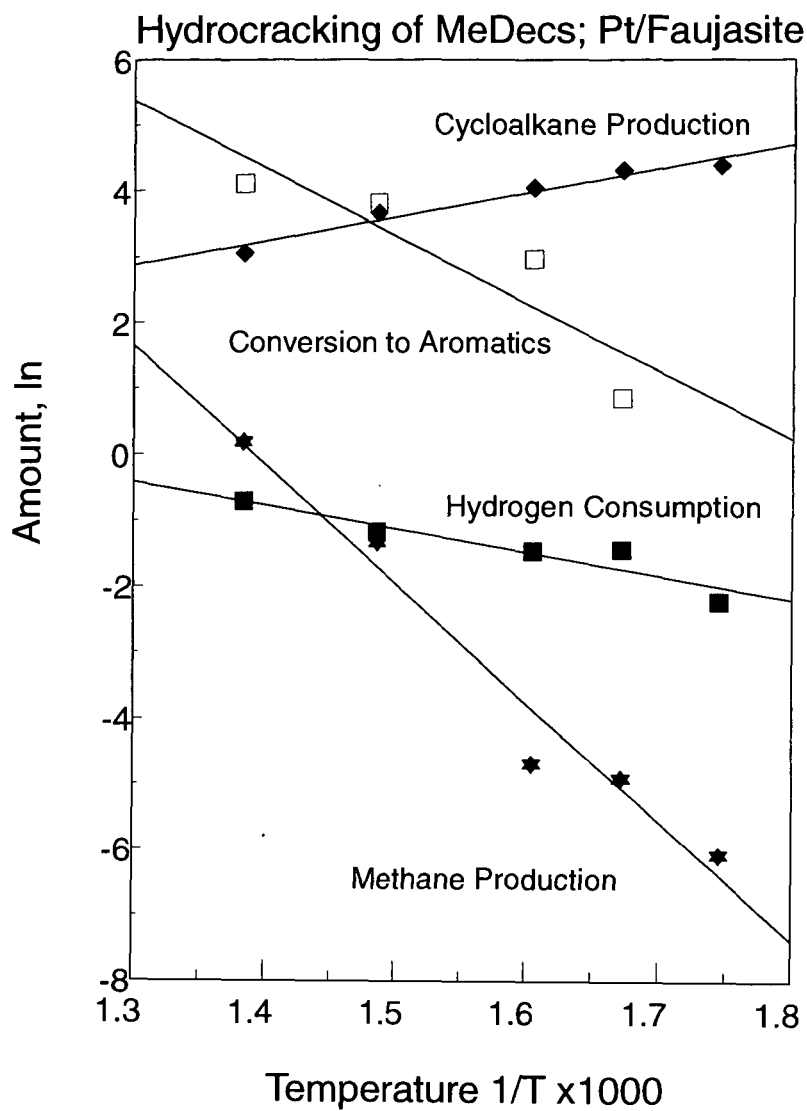


Figure 1.
Hydrocracking of Methyldecals over Pt/Faujasite. 700 psi. 1h. 10:1 Feed to Catalyst Ratio.

Hydrocracking of MeDecs; Pd/Faujasite

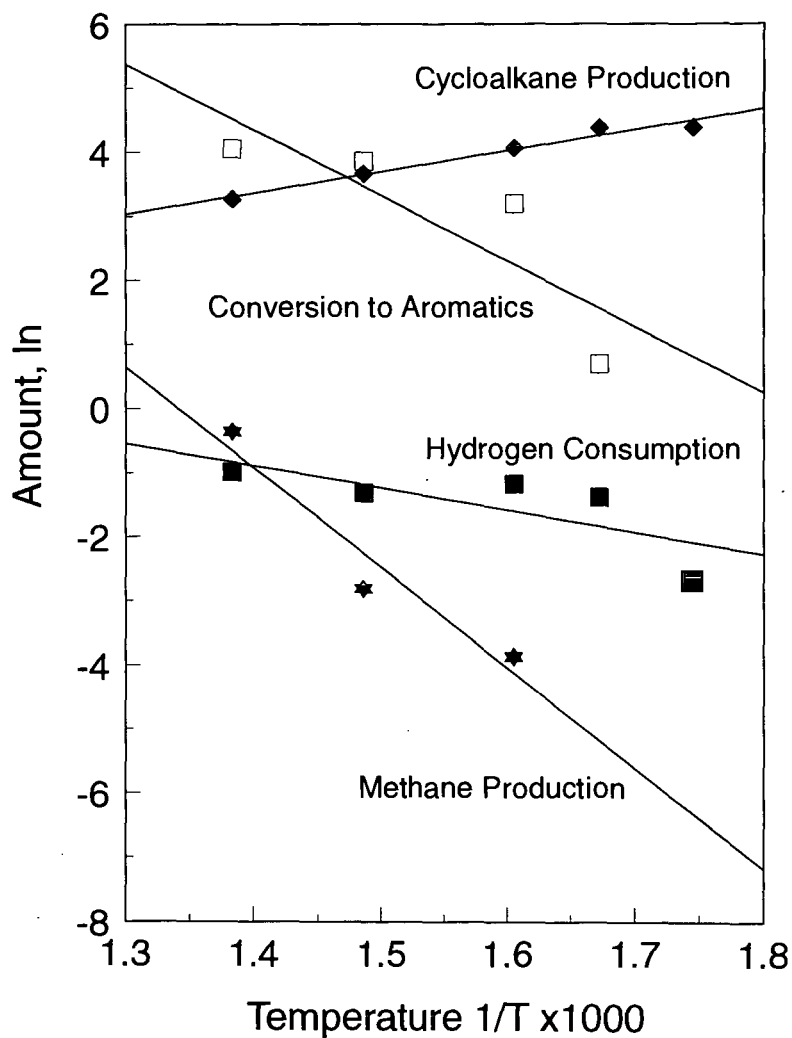


Figure 2.
Hydrocracking of Methyldecals over Pd/Faujasite. 700 psi. 1h. 10:1 Feed to Catalyst Ratio.

REACTION BEHAVIORS OF MIXED PLASTICS IN LIQUID-PHASE CRACKING

Jyi-Perng A. Wann, Tohru Kamo, Hiroshi Yamaguchi*, and Yoshiki Sato
National Institute for Resources and Environment, Tsukuba, Ibaraki, 305 Japan
*Engineering Research Center, NKK Corp., Kawasaki, Kanagawa, 210 Japan

Keywords: PS, PE, Liquefaction

INTRODUCTION

The majority of waste plastics today is either incinerated or buried for landfills. However, incineration of waste plastics can cause damages in furnace and air pollution problems. Shortage of available landfill sites also has become a serious concern. The methods of waste plastic recycling therefore have been paid much attention with the viewpoint of effective environmental protection. Liquefaction of waste plastics is an attractive recycling method in terms of producing fuel oil or chemicals. To date, most of the waste plastic liquefaction investigations have been limited to the areas not involving the use of a solvent. Pilot-scaled plants, such as those in the Fuji Recycle Process in Japan [1] and the VCC Process in Germany [2], have been operated for some time. Although high conversion of waste plastics can be obtained at a temperature as low as 400 °C, problems such as wide molecular weight distribution in the produced oil and high coking tendency have been encountered. Liquid-phase cracking of waste plastics has the potential of overcoming these problems, yet few research has been reported on the liquefaction behaviors for the liquid-phase cracking [3-5]. Polyethylene (PE) has been regarded as one of the polymers difficult to liquefy, while the cracking of polystyrene (PS) is considered to proceed in a way different from that of PE. Hence, we investigated the cracking of PS, PE, and their mixtures using solvents of different hydrogen donation capability. Differences in the liquefaction behaviors between PS and PE, influences of the solvent type, synergistic effects for the liquefaction of PS/PE mixtures, and a property in the oil are presented in this paper.

EXPERIMENTAL

Pellet-sized high-density PE (Mitsui Petrochemical Co.) and PS (Dai-Nippon Ink Chemicals) of commercial grades were used. Reagent-grade tetralin (>97% purity) and n-decane (>99% purity) (Tokyo Chemical Industry Co.) were used without further purification. A total weight of 80 g of the plastic-solvent mixture was charged into a 300-mL autoclave reactor in each run. The wt./wt. ratio between the plastic and the solvent was 1/3 or 1/0. For the liquefaction of plastic mixtures, the wt./wt. ratio of PS to PE used was 3/1, 1/1, or 1/3. The reactor was charged with nitrogen to 40 kg/cm² (570 psig) at room temperature. The reaction was conducted at 440 °C for 60 min, with constant stirring at 1000 rpm. The volume and the composition of the produced gases were measured after reaction. The produced liquid, of which the weight was calculated based on the assumption of no weight loss for light products at room temperature, was distilled under a vacuum less than 1 torr. The recovered liquid, with the boiling point range lower than 538 °C, was further analyzed with a GC-FID system equipped with a capillary column. The oil yield was calculated with the following equation:

$$\text{Oil yield, (wt./wt. basis)} = \frac{\text{wt. (recovered liquid)} - \text{wt. (charged solvent)}}{\text{wt. (charged plastic)}}$$

Concentrations of, mainly, benzene, toluene, and some alkylbenzenes and n-alkanes, were measured by the FID-GC analysis.

RESULTS AND DISCUSSION

Cracking of PS

The yields of products from PS cracking at 440 °C, with and without solvent addition, are presented in Table 1. The results for corresponding solvent blank runs are also included for comparison. In the absence of a solvent, the yields of gas, oil, and residue were 0.3, 72.9, and 26.8%, respectively. Toluene, ethylbenzene, and cumene were the main liquid products from PS. Benzene, styrene, and n-propylbenzene were produced in relatively low quantities. We found that a much higher molar quantity of toluene was produced than that of methane. This suggests that the majority of the toluene may not come directly from the cracking of ethylbenzene.

When n-decane was used, the yields of gas, oil, and residue were 5.1, 83.8, and 11.1%, respectively. Under the reaction condition, n-decane was expected to be an

inert solvent, because only a small amount of n-alkanes in C5–C9 range was produced during the n-decane solvent blank run. Nevertheless, a slight increase in the total yield of gas, which includes ethane, propane, and n-butane that can be converted from n-decane, has been observed in the reaction with PS. The increased gas yield indicates that the presence of PS may have enhanced the decomposition of n-decane slightly. The higher oil yield, when compared to the case without the solvent addition, suggests that the occurrence of condensation reactions may be decreased by a dilution effect from n-decane solvent.

The highest oil yield of 95.8% was obtained when tetralin was the solvent. This could be due to both the effects of solvent dilution and hydrogen donation from tetralin solvent.

Cracking of PE

Table 2 shows the distribution of products from PE cracking at 440 °C. Without the solvent addition, the yields of gas, oil, and residue were 1.7, 53.9, and 44.4%, respectively. The characteristic distribution of n-alkanes in the produced oil indicates that the decomposition of PE proceed by radical chain reactions [1]. Very low oil yields of 1.6% and 0.8% were obtained for the cracking in n-decane and in tetralin, respectively. The decreased conversion of PE with n-decane may be due to a retardation effect resulting from solvent dilution to the induced cracking of PE. The lowest conversion of PE, obtained in tetralin, suggests that the combined effects of dilution and hydrogenation by tetralin may have further retarded the decomposition of PE.

Cracking of PS/PE Mixtures

No solvent addition. Figure 1 shows the yields of toluene, ethylbenzene, cumene, n-alkanes in C5–C9 range, and oil yield in the reaction without solvent addition. At each PE fraction (as expressed by PE/(PE+PS) in Figures 1–3) of 0.25, 0.50, and 0.75, the oil yield of the plastic mixtures was higher than that of each comprising plastic. The fairly constant yield of toluene and the slight decreased yield of ethylbenzene, as observed for the PE fractions from 0 to 0.50, suggests that cracking of PS may have been enhanced by the mixing from PE. The total yield of n-alkanes in C5–C9 range produced from PE was low but increased proportionally with the increasing amount of PE in the feed mixtures. This indicates that the presence of PS did not enhance the cracking of PE. Therefore, it is considered that the enhanced conversion of PS to oil could be mainly due to a dilution effect resulted from PE, similar to that from n-decane to the cracking of PS, as discussed earlier.

n-Decane as the solvent. Figure 2 shows the effect of n-decane on the distribution of products due to PE and PS mixing. The figure shows significant synergistic effects for oil yields in the mixtures. The yields of toluene, ethylbenzene, and cumene decrease almost linearly with the increased PE fraction in the feed mixtures. The trend for the products implies that cracking of PS may not be significantly enhanced by the presence of PE. The high synergistic effect for oil yield at the PE fraction of 0.75 could be mainly due to the enhanced contribution from PE cracking since the dilution effect from the solvent may be considered equal for all the fractions. The yield of C5–C9 n-alkanes was fairly constant in the PE fraction ranges from 0 to 0.75. This indicates that the n-alkanes may be produced from the decomposition of n-decane, PE, or the both.

Tetralin as the solvent. Figure 3 shows the effect of tetralin on the distribution of products due to PE and PS mixing. The yields of oil and each light aromatic compound from PS decreased monotonously with the increased PE fraction. The results also show that the effects of tetralin for oil yield increases in the mixtures were not as pronounced as in the aforementioned two cases. The nearly linear relationship between the yields of each products at each PE fraction indicates that the synergistic effects between PS and PE could be low in tetralin solvent. It may be a result of rapid stabilization by hydrogen donation from tetralin to the radicals produced from PS cracking.

CONCLUSIONS

The use of solvents can play important roles in the liquefaction of plastics. For the liquid-phase cracking of PS, it has been demonstrated that the oil yield can be

increased by the minimization of condensation reactions. On the other hand, the oil yield for PE cracking can be decreased as a result of retardation to radical chain reactions, due to the dilution or hydrogen donation effect from the solvents. Interactions between PS and PE also can be influenced by the solvents used. Liquid-phase cracking shows a promising direction for the processing of waste plastics by proper selection of reaction systems.

ACKNOWLEDGMENTS

One author, J.-P. Anthony Wann, would like to thank the financial supports of STA fellowship arranged by National Science Foundation, USA, and Science and Technology Agency, Japan. He is also grateful to the helpful discussion from Professor David M. Bodily of University of Utah.

REFERENCES

1. Kasutani, T., et al., Waste Plastics – Thermal and Chemical Recycling, Kagaku Kogyo Nippo Sha, Tokyo, Japan, 1994. p. 9.
2. Niemann K., "Feedstock Recycling of Post Consumer Waste Plastics," Proceedings Recycle '95 – Environmental Technologies, p. 5-3.1.
3. Palmer, S. R., Hippo, E. J., Tandon, D., and Blankenship, M., "Liquefaction of Coal/Waste Plastic Mixtures" Proc. 8th Int. Conf. of Coal Sci., 1995, Elsevier, Amsterdam, Vol. II, p. 1523.
4. Huffman, G. P., Feng, Zhen, Huggins, F. E., and Mahajan, V., "Direct Liquefaction of Waste Plastics and Coliquefaction of Waste Plastics with Coal," Proc. 8th Int. Conf. of Coal Sci., 1995, Elsevier, Amsterdam, Vol. II, p. 1513.
5. Burgdorf, J., and Kocker, H. Meier zu, "Hydrogenating Liquefaction of Plastic Wastes in Hydrogen-Donating and Non-Hydrogen-Donating Solvents," Ber.-Dtsch. Wiss. Ges. Erdoel, Erdgas Kohle, Tagungsber, 1994, p. 353.

Table 1. Yields of products from blank runs and from PS cracking at 440 °C

Reaction Environment:		Tetralin		n-Decane		No Solvent
	wt. % of PS	Blank ¹⁾	440 °C	Blank ¹⁾	440 °C	440 °C
Gas		0.0	0.7	2.1	5.1	0.3
Oil			95.8		83.8	72.9
benzene		0.0	0.2	0.0	0.7	0.9
toluene		0.2	40.8	0.0	33.3	21.6
ethylbenzene		0.2	27.7	0.0	13.4	27.4
styrene		0.0	0.5	0.0	0.5	0.0
cumene		0.0	5.5	0.0	3.7	6.6
n-propylbenzene		0.0	1.5	0.0	1.6	1.3
<u>total light aromatics</u>		0.4	76.2	0.0	53.1	57.8
<u>total C5–C9 n-alkanes</u>		0.0	0.0	7.8	1.0	0.1
Residue			3.5		11.1	26.8

Note: 1) data calculated on the basis of the initial weight of plastic

Table 2. Yields of products from PE cracking at 440 °C

Reaction Environment:		Tetralin	n-Decane	No Solvent
	wt. % of PE			
Gas		0.1	0.8	1.7
Oil		0.8	1.6	53.9
<u>total C5–C9 n-alkanes</u>		0.0	3.2	6.8
Residue		99.1	97.6	44.4

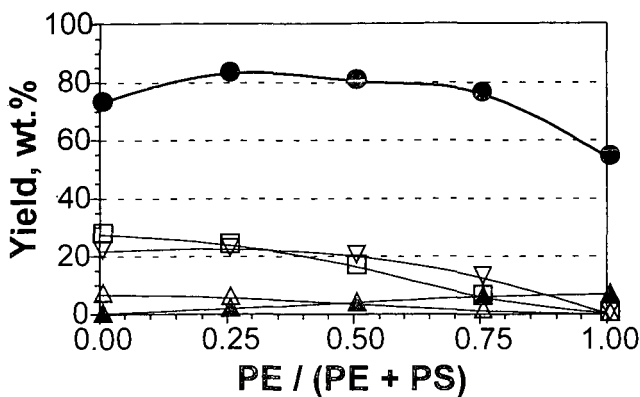


Figure 1. Effect of plastics mixing on yields of products without solvent

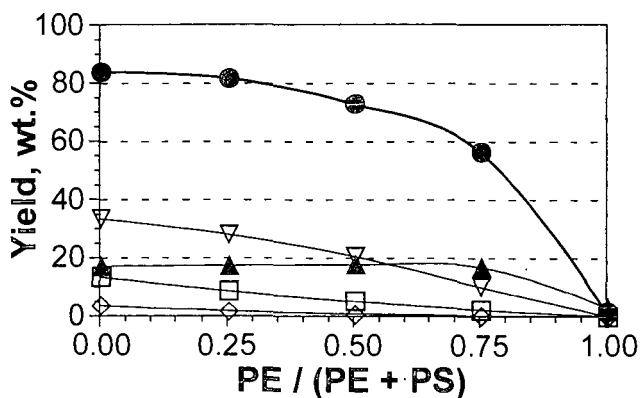


Figure 2. Effect of n-decane on yields of products due to PS-PE mixing

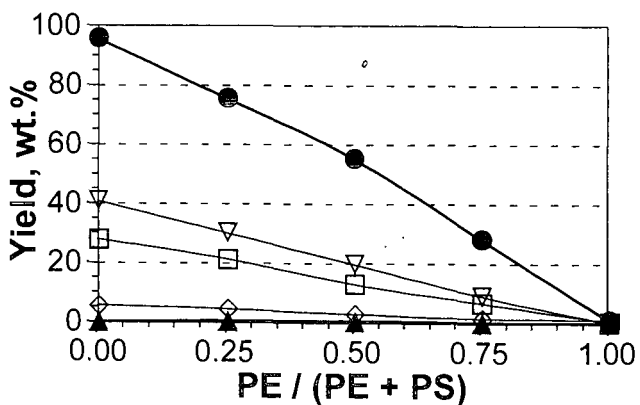


Figure 3. Effect of tetralin on yields of products due to PS-PE mixing

CATALYTIC CRACKING OF POLYSTYRENE

Rong Lin and Robert L. White
Department of Chemistry and Biochemistry
The University of Oklahoma, Norman, OK 73019

Keywords: catalytic cracking, polymer cracking, polymer recycling

Introduction

Plastics have become the most produced materials in the United States since the mid of 1970's. The significant increase in plastics production has resulted in a similar significant increase in plastics disposal. Polystyrene is widely used in consumer product packaging and to make disposable containers. About one billion pounds of polystyrene are used in single-use disposable applications.

One approach to deal with plastic waste is to convert it into useful products, such as fuel oil and chemicals^[1,2], by tertiary recycling methods. The development of effective plastic waste recycling by catalytic cracking will require detailed knowledge of the relationship between catalyst structure and cracking product distributions^[3-7]. In order to compare the polymer cracking properties of different catalysts, it is preferable to examine the effects of catalysts without complications due to reactions of primary cracking products with polymer residue. Secondary reactions can be minimized by limiting the contact between primary volatile products and the catalyst/polymer mixture. This can be accomplished by maintaining high catalyst to polymer ratios and providing efficient and rapid removal of volatile products. In this paper, the importance of catalyst acidity and HZSM-5 channel structure on the volatile catalytic cracking product distributions derived from polystyrene is assessed by comparing thermal analysis results obtained from samples prepared by coating silica-alumina, HZSM-5 zeolite, and sulfated zirconia catalysts with thin layers of polystyrene.

Experimental

Samples examined in this study were: high molecular weight polystyrene (HPS), low molecular weight polystyrene (LPS), and polystyrenes coated on silica-alumina, HZSM-5, and sulfated zirconia cracking catalysts (10-20% (wt/wt)). HPS and LPS were purchased from Aldrich Chemical Company (Milwaukee, WI). The silica-alumina catalyst was provided by Condea Chemie GmbH (Hamburg, Germany). The silica-alumina catalyst contained 11.8% by weight alumina and had a surface area of 282 m²/g. The HZSM-5 zeolite catalyst was obtained from Mobil Oil (Paulsboro, NJ) and was characterized by a 355 m²/g surface area and a 1.5% alumina content. The sulfated zirconia catalyst was synthesized following procedures described previously. The sulfated zirconia catalyst had a surface area of 157 m²/g and contained 9% by weight sulfate. Polystyrene-catalyst samples were prepared by dissolving polystyrene in cyclohexane, adding catalyst, and then rotoevaporating the mixture to remove solvent. The resulting polymer coated catalyst samples were dried for several hours at 90°C. The apparatus used for pyrolysis-GC/MS and TG-MS measurements have been described previously. Pyrolysis separations were achieved by using a HP 5890 capillary GC with a DB-5 column (0.25 μ m film thickness). The gas chromatograph oven temperature program consisted of a 2 min isothermal period at -50 °C followed by a 10 °C/min ramp to 280 °C, and then another isothermal period at 280 °C for 5 minutes. For TG-MS studies, samples were heated from 50 °C to 600 °C in He at rates of 1, 10, 25, and 50 °C/min. For TG-GC/MS studies, a Valco Instruments, Inc. (Houston, TX) heated eight external volume sample injector was employed to divert small volumes (ca. 20 μ L) of TG effluent into a 30 m DB-5 capillary column (0.25 μ m film thickness) for GC/MS analysis. A 5 °C/min heating rate from 50 °C to 600 °C in 20 mL/min He was used to heat samples in the thermogravimetric analyzer. When samples reached 100 °C, TG effluent was sampled. Above 100 °C, TG effluent sampling was repeated at 3 min intervals during TG-GC/MS analysis. A 5 mL/min He carrier gas flow rate through the TG-GC/MS chromatographic column was employed and the column temperature was maintained at 100 °C during separations. TG-GC/MS column effluent was split prior to entering the mass spectrometer to maintain an ion source pressure of 5 x 10⁻⁵ torr.

Results and Discussion

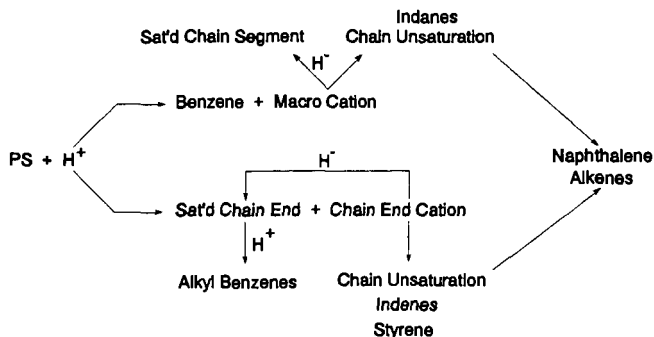
Pyrolysis-GC/MS results obtained for polymers and polymer-catalyst samples pyrolyzed at 400°C were compared to investigate the effects of different catalysts and initial polymer molecular weight on cracking product distributions. Tables 1 and 2 contain the volatile product distributions derived from chromatograms for neat polymers and polymer-catalyst samples. Thermal degradation of neat polystyrene samples produced primarily styrene monomer along with substantial amounts of dimer and trimer. By examining the volatile product distributions for high molecular weight polystyrene (HPS) and low molecular weight polystyrene (LPS), it was found that the relative yield of trimer was about three times that of the dimer and the relative yield of styrene was greater for the HPS sample than for the LPS sample. However, in the presence of catalysts, the most abundant volatile product was benzene, and very little styrene was detected. Benzene comprised about 30% of the volatile material produced from the polymer-Si/Al and polymer-ZrO₂/SO₄ samples, and over 50% from the polymer-HZSM-5 zeolite samples. Other volatile products detected from the polymer-catalyst samples with relative yields over 1% included: alkyl benzenes, indanes, indenenes, and naphthalenes. For both LPS and HPS samples, the relative yields of alkyl benzenes were greatest for samples containing Si/Al and ZrO₂/SO₄ catalysts, whereas polymer-HZSM-5 samples produced fewer alkyl benzenes but significantly larger quantities of indenenes.

TG-MS was employed to correlate the evolution of volatile thermal decomposition products with sample weight loss and to calculate volatilization activation energies. Weight loss curves obtained by heating samples at 10 °C/min in He are shown in Figures 1 and 2. Compared to neat polymer thermal decompositions, all three catalysts lowered the temperature at which significant sample weight loss occurred. The catalytic effect was greatest for the samples containing the ZrO₂/SO₄ catalyst. By examining the weight loss curves, it was found that, for the same catalysts, the weight loss onset temperature was lower for the LPS polymer than for the HPS polymer. The polymer-ZrO₂/SO₄ samples exhibited two distinct steps in their weight loss curves. TG effluent mass spectra indicated that the low temperature weight loss step was caused by polystyrene decomposition. The high temperature step resulted from catalyst decomposition and corresponded to SO₂ evolution.

Neat polymer and polymer-catalyst samples were subjected to TG-MS analysis in He with heating rates of 1, 10, 25, and 50 °C/min to investigate the effects of catalysts on volatilization activation energies calculated by using the Friedman method. The activation energy for the neat HPS polymer was slightly higher than that for the neat LPS polymer. For samples containing the same catalyst, those containing the LPS polymer exhibited a lower volatilization activation energy than those containing the HPS polymer. The lowest volatilization activation energies were calculated for samples containing ZrO₂/SO₄ catalyst.

Mass spectra obtained during TG-MS analyses could not be used to profile the temperature dependent evolutions of the primary thermal decomposition products because species specific ions could not be identified. By placing a gas chromatograph between the thermogravimetric analyzer and mass spectrometer, it was possible to separate the primary volatile products generated in the thermogravimetric analyzer prior to mass analysis. Figures 3 and 4 contain plots of TG-GC/MS chromatographic peak areas (integrated total ion current) as a function of sample temperature for selected products. For all samples analyzed, benzene was by far the most abundant volatile product. All of the polymer-catalyst samples produced alkyl benzenes and indanes, however samples containing HZSM-5 catalyst produced significantly less than the other samples. Styrene and indenenes were only detected from samples containing HZSM-5 catalyst.

Formation of the primary polystyrene catalytic cracking volatile products can be explained by consequences of initial electrophilic attack on polymer aromatic rings by protons. Most of the products detected by pyrolysis-GC/MS and TG-GC/MS can be derived from ortho ring protonation. The initial step in polystyrene cracking is protonation of polymer aromatic rings. Ortho protonation can easily lead to benzene evolution and the formation of a secondary macro cation, or may result in chain shortening, yielding a chain end cation and a saturated chain end.



After protonation of chain end aromatic rings, β -scission can yield alkyl benzenes. Beta-scission and rearrangement of chain end cations can lead to chain unsaturation or the formation of styrene and indenenes. Cyclization of the secondary macro cations can lead to the formation of indenenes, or after rearrangements and β -scission of macro cations, chain unsaturation can be formed. Also, macro cations can undergo hydride abstraction leading to the formation of saturated chain segments. A consequence of chain unsaturation might be the formation of conjugated polyene segments that may subsequently cyclize to form naphthalenes.

Conclusions

Effects of different catalysts and initial molecular weights of polystyrene on catalytic cracking product distributions were studied. Benzene was produced by polystyrene catalytic cracking at temperatures as low as 130 °C for LPS-ZrO₂/SO₄ samples. This suggests that low temperature benzene evolution may result primarily from chain ends, which would be more abundant for the LPS polymer than for the HPS polymer. Chain end aromatic rings should be somewhat more susceptible to electrophilic attack because electron release from the polymer backbone into these rings should be slightly greater than for other aromatic rings in the polymer. Because the samples containing the LPS polymer had more chain ends than the HPS polymer, low temperature reaction rates for the LPS polymer would be consistently higher than for the HPS polymer, which would lead to the observed higher benzene evolution rates at low temperature for samples containing the LPS polymer. Benzene can be easily formed after aromatic ring protonation, but that formation of other volatile products is more difficult and may require additional reactions, such as macro cation rearrangement, hydride abstraction, or successive protonations.

Acknowledgment

Financial support for this work from the National Science Foundation (CTS-9509240) is gratefully acknowledged.

References

1. D.S. Scott, S.R. Czernik, J. Piskorz, D. Radlein, *Energy & Fuels*, **4**, 407(1990).
2. Y. Ishihara, H. Nambu, T. Ikemura, T. Takesue, *J. Appl. Polym. Sci.*, **38**, 1491(1989).
3. M. Yamamoto, I. Suzuko, S. Yamanaka, *Nippon Kagaku Kaishi*, **5**, 802(1976).
4. T. Ogawa, T. Kuroki, S. Ide, T. Ikemura, *J. Appl. Polym. Sci.*, **27**, 857(1981).
5. Cr.I. Simionescu, C. Vasile, P. Onu, M. Sabliovschi, G. Moroi, V. Barboiu, D. Ganju, M. Florea, *Thermochim. Acta*, **134**, 301(1988).
6. Z. Zhang, T. Hirose, S. Nishio, Y. Morioka, N. Azuma, A. Ueno, H. Ohkita, M. Okada, *Ind. Eng. Chem. Res.*, **34**, 4514(1995).
7. G. Audisio, F. Bertini, P.L. Beltrame, P. Carniti, *Polym. Degrad. Stab.*, **29**, 191(1990).

Table 1. LPS Decomposition Products at 400°C

Product	Neat LPS	LPS-Si/Al	LPS-ZrO ₂ /SO ₄	LPS-HZSM-5
benzene		31	31	52
toluene	1	1	3	3
ethyl benzene		20	10	5
styrene	41	1		1
isopropyl benzene		6	6	
methyl styrene				
indane		10	10	7
indene		1		3
methyl indane		17	25	7
methyl indene				3
naphthalene		4	2	7
2-methyl naphthalene		4	2	6
1-methyl naphthalene		2	2	
dimer	11			
trimer	35			

Table 2. HPS Decomposition Products at 400°C

Product	Neat HPS	HPS-Si/Al	HPS-ZrO ₂ /SO ₄	HPS-HZSM-5
benzene		30	33	60
toluene			3	2
ethyl benzene		14	12	2
styrene	68	4		2
isopropyl benzene		9	8	
methyl styrene				1
indane		15	9	3
indene		1		3
methyl indane		17	8	6
methyl indene				3
naphthalene		3	7	3
2-methyl naphthalene		2	5	3
1-methyl naphthalene		2	5	1
dimer	6			
trimer	16			

Table 3. Volatilization Activation Energies (kcal/mol)

Catalyst	LPS	HPS
none	46.4 ± 1.2	48.5 ± 0.8
Si-Al	33.8 ± 0.5	38.6 ± 0.5
ZrO ₂ /SO ₄	24.4 ± 2.9	28.9 ± 1.9
HZSM-5	34.6 ± 0.5	36.0 ± 1.3

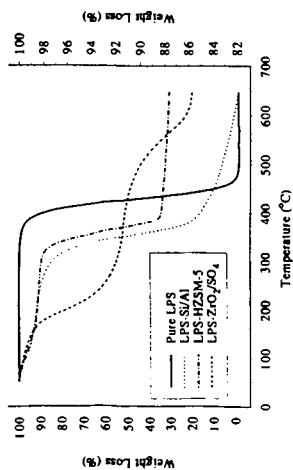


Figure 1. TG weight loss curves for neat LPS (left axis) and LPS-catalyst samples (right axis) obtained by heating samples at a rate of 10 °C/min.

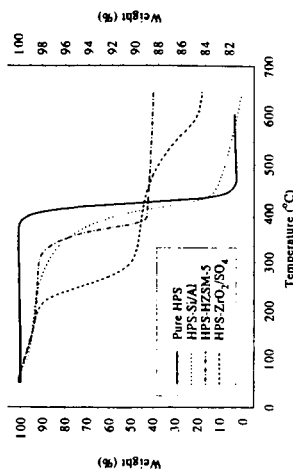


Figure 2. TG weight loss curves for neat HPS (left axis) and HPS-catalyst samples (right axis) obtained by heating samples at a rate of 10 °C/min.

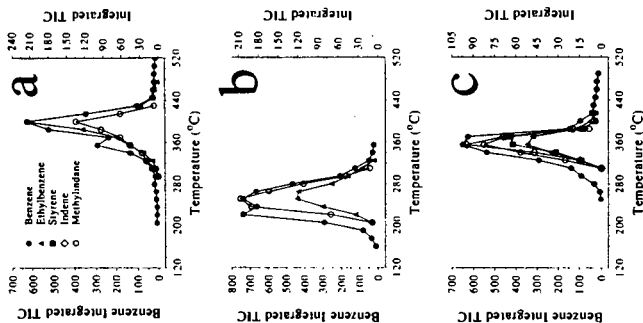


Figure 3. TG-GC/MS chromatographic peak areas derived from (a) LPS-Si/Al, (b) LPS-ZrO₂/SO₄, and (c) LPS-HZSM-5.

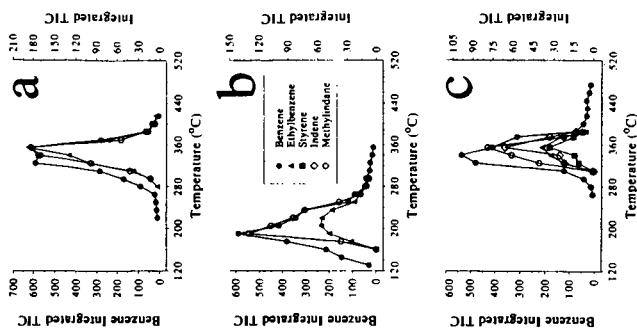


Figure 4. TG-GC/MS chromatographic peak areas derived from (a) HPS-Si/Al, (b) HPS-ZrO₂/SO₄, and (c) HPS-HZSM-5.

INFLUENCE OF METAL OXIDE MODIFICATION OF ALUMINA ON THE DISPERSION AND ACTIVITY OF VANADIA CATALYSTS

L. Jhansi Lakshmi and Elmer C. Alyea

Department of Chemistry and Biochemistry
University of Guelph, ON N1G 2W1

and

S.T. Srinivas, P.S. Sai Prasad and P. Kanta Rao

Physical and Inorganic Chemistry Division
Indian Institute of Chemical Technology
Hyderabad-5000 007, A.P., India

Alumina was modified with 10% MO_x ($\text{MO}_x = \text{TiO}_2, \text{ZrO}_2, \text{La}_2\text{O}_3$ or MgO) prior to its impregnation with 12 wt% vanadia. The catalysts were characterised by x-ray diffraction (XRD), electron spin resonance (ESR) and oxygen chemisorption. The activities of the catalysts were determined by methanol partial oxidation and their acid-base properties were evaluated for the decomposition of isopropanol. Metal oxide modification is found to influence significantly the surface coverage and the methanol partial oxidation activity of vanadia supported on alumina. With proper MO_x modification enhanced reducibility of vanadia could be attained, which in turn makes the partial oxidation more facile.

Keywords: modified alumina, vanadia, partial oxidation

INTRODUCTION

Vanadia supported on high surface area carriers like Al_2O_3 , SiO_2 , etc., has been widely studied for catalyzing a great variety of reactions such as partial oxidation, selective catalytic reduction of NO_x and oxidative dehydrogenation of light alkanes [1-5]. The oxides like TiO_2 and ZrO_2 when employed as supports for partial oxidation and hydroprocessing catalysts, were found to exhibit enhanced activities and selectivities in comparison with Al_2O_3 -supported catalysts [2,6]. The disadvantages with these carriers are their low surface area, high surface acidity, low volume activity and phase transition at high temperatures making them unsuitable for industrial applications. By adding small quantities of these oxides to relatively high surface area, thermally stable supports such as alumina the aforesaid problems can be obviated. Recently there are reports in the literature [7-11] on the support modification with additives like alkali/alkaline earth metals, halides, rare earth oxides, phosphates and sulphates, which enhance the acidic or basic character or impart thermal stability to the carrier. Shen et al. [7,8] in their investigations on Al_2O_3 support modification with additives such as K_2O , MgO , La_2O_3 , SnO_2 etc. have observed that these oxides influence the number and nature of acid sites on alumina support surface. Wei et al. [12] have observed increased reducibility of molybdena and higher hydrodesulphurisation activity on titania modified $\gamma\text{-Al}_2\text{O}_3$ supported hydroprocessing catalysts. Support modification is said to influence the nature of active sites by way of increasing the reducibility of the transition metal oxide resulting in enhanced activity and selectivity of the catalysts. However, the influence of support modification on the redox and acid-base properties of $\text{V}_2\text{O}_5/\text{Al}_2\text{O}_3$ is not yet thoroughly understood.

The aim of the present investigation is to elucidate the role of modification of the Al_2O_3 support with TiO_2 , ZrO_2 , La_2O_3 or MgO on the dispersion and methanol partial oxidation activity of vanadia catalysts.

EXPERIMENTAL

Four different modified supports, namely, TiAl , ZrAl , LaAl and MgAl were prepared by impregnating the $\gamma\text{-Al}_2\text{O}_3$ (Harshaw, Gamma phase, S.A. 196 m^2/g) support with 10 wt. % each of MO_x , ($\text{MO}_x = \text{TiO}_2, \text{ZrO}_2, \text{La}_2\text{O}_3, \text{MgO}$). The precursors used were Fluka A.R. grade $(\text{C}_{12}\text{H}_{28}\text{O}_4)\text{Ti}$ and $(\text{C}_{12}\text{H}_{28}\text{O}_4)\text{Zr}$ for TiO_2 and ZrO_2 respectively; and Loba Chemie, A.R. grade $\text{Mg}(\text{NO}_3)_2$, $6\text{H}_2\text{O}$ and $\text{La}(\text{NO}_3)_3$, $6\text{H}_2\text{O}$ for MgO and La_2O_3 , respectively. The organometallic precursors of titania and zirconia were dissolved in methanol prior to impregnation on Al_2O_3 . Lanthanum and magnesium hydroxides were precipitated by ammonia hydrolysis of their aqueous nitrate solutions. The excess solutions were evaporated to dryness on a water bath and the catalyst masses were further dried in an air oven at 110°C for 12 h. The modified supports were calcined at 550°C for 5 h. VMAI catalysts ($\text{M} = \text{Ti}, \text{Zr}, \text{La}, \text{Mg}$) were synthesized by

impregnation of aqueous solution containing a calculated amount of NH_4VO_3 (Fluka, A.R. grade), corresponding to 12 wt.% V_2O_5 , on modified supports. Drying and calcination procedures were similar to those described above. Following the same procedure a 12 wt.% $\text{V}_2\text{O}_5/\text{Al}_2\text{O}_3(\text{VAI})$ was prepared as a reference.

XRD patterns were recorded on a Phillips PW 1051 diffractometer using Ni filtered CuK_α radiation. ESR spectra were recorded on a Bruker ER 200 D SRC X band spectrometer with 100 KHz modulation at ambient temperature. An all-glass high vacuum apparatus with a facility to reduce (at 500°C , in a flow of H_2) the samples *in situ* was used to carry out the low temperature (-78°C) oxygen chemisorption experiments. The details of the experimental procedure are described elsewhere [10]. BET surface area of the catalysts were determined by N_2 physisorption.

Activity studies for the partial oxidation of methanol were carried out in the temperature range $175\text{--}250^\circ\text{C}$ taking 200 mg of the catalyst (0.5 mm size) packed in a fixed bed tubular glass reactor of 6 mm i.d. Purified air at a flow rate of 60 ml/min, saturated with methanol (by passing through a saturator maintained at 25°C), was introduced into the reactor. After a steady-state period of 30 min the products were analyzed on-line with a 10% Carbowax 20 M column (2 m long) using a flame ionization detector. The product stream comprised mainly formaldehyde, dimethyl ether with some traces of methyl formate, CO and CO_2 . Oxidative decomposition of isopropanol was carried out in the same reactor under similar reaction and analysis conditions at a constant temperature of 175°C and at atmospheric pressure, using about 200 mg of catalyst. The products observed consisted mainly of propene and acetone with traces of diisopropyl ether.

RESULTS AND DISCUSSION

BET surface area, oxygen uptake, active site density and surface coverage values are shown in Table 1. It can be seen that the surface areas of the vanadia catalysts supported on MO_x modified alumina (VMAI) are significantly lower than vanadia on unmodified alumina (VAI), which in turn, is lower than the alumina support itself. This observation is expected due to the blockage of pores in the alumina as a result of the addition of the metal oxide as well as the active component. Oxygen uptakes of the VMAI catalysts are more when compared to the VAI catalyst except in the case of VMgAl. Among the four catalysts VTiAl is showing the highest oxygen uptake which may be due to a greater number of reducible vanadia sites. Both active site density and the surface coverage are high in VTiAl indicating that the V_2O_5 is highly dispersed on the TiO_2 modified Al_2O_3 support. Generally the strength of interaction between the support and the active component governs the dispersion and hence oxygen uptake capacity [13]. The increased oxygen uptakes of VTiAl, VZrAl and VLaAl catalysts may be due to reduced strength of metal oxide-support interaction. Modification of alumina might have caused a decrease in interaction between the support and active phase enabling increased reducibility of V_2O_5 . Similar observations were made by Wei et al. in molybdena based hydroprocessing catalysts supported on TiO_2 modified Al_2O_3 [12].

The XRD patterns of the VAI and VMAI catalysts show that there are no lines corresponding to crystalline vanadia in all the catalysts. Vanadia may be existing as a highly dispersed phase. However, the presence of microcrystalline particles with size less than 40 Å cannot be ruled out. The modified supports exhibited the peaks corresponding to their respective oxides with low intensities. The anatase phase of TiO_2 was observed in TiAl and lines corresponding to tetragonal and monoclinic phases of ZrO_2 were observed in ZrAl. LaAl and MgAl were x-ray amorphous.

Fig. 1 shows the ESR spectra of various catalysts recorded at ambient temperature. Clear hyperfine splitting (hfs) corresponding to V^{4+} can be seen in VTiAl and VZrAl indicating the isolation of vanadia species on the surface of the support. This is a significant observation since the hfs of vanadia species vanadia supported on unmodified Al_2O_3 has been reported to be recorded only at liquid nitrogen temperature [14]. The observance of hyperfine interaction only at -196°C implies that it is destroyed by spin-spin interaction at higher temperatures between neighboring V^{4+} ions. The resolution of peaks is not so discrete in the cases of VLaAl and VMgAl indicating possible agglomeration of V^{4+} ions leading to dipolar broadening.

The conversions and selectivities towards formaldehyde and dimethylether on various catalysts in partial oxidation of methanol (carried out at a reaction temperature of 200°C) are plotted in Fig. 2. The activities of VMAI catalysts are in the order $\text{VTiAl} > \text{VZrAl} > \text{VLaAl} > \text{VMgAl}$. The O_2 uptakes of the catalysts also varied in a similar manner indicating that the active sites titrated by oxygen molecules are responsible for the observed activities of the catalysts. Active sites are the vacancies created by removal of labile oxygen atoms (by reduction) upon which the

dissociative chemisorption of oxygen takes place. Selectivity towards the dehydrogenation product, HCHO, has been improved over the VAl catalyst.

Deo and Wachs [2] in their investigation on partial oxidation activity on supported vanadia catalysts have reported that instead of the weakening of the V=O bond, it is the weakening of the vanadium-oxygen-support bridging bond that is responsible for the activity. Our results indicate that the increased oxygen uptake capacities of vanadia on TiO₂, ZrO₂ and La₂O₃ modified alumina catalysts are a consequence of reduced strength of metal-support interaction. Interaction of V₂O₅ with MgO appears to be stronger compared to the oxide support interaction in the cases of VAl and the other VMAl catalysts, which leads to reduced oxygen uptake and hence the partial oxidation activity.

Supported vanadia catalysts exhibit bifunctional character since they possess both acid-base and redox sites. The influence of MO_x modification on the acid-base properties of the catalysts have been examined by the isopropanol decomposition reaction. The results are incorporated in Table 1. Relatively higher decomposition rates have been obtained on VTiAl, VZrAl and VLaAl compared to VAl catalyst. But, when compared to VAl, the acetone selectivities of the above three catalysts have decreased by 15-25%. However, the sustained predominance of selectivity to acetone over selectivity to propylene indicates that in these catalysts the redox property is more dominant than their acid-base character. However, in the case of VMgAl the lower decomposition activity associated with maximum dehydrogenation selectivity could be mainly due to the generation of acid-base paired sites which act in a concerted manner as proposed by Bond et al. [15]. Low oxygen uptake, a consequence of low reducibility, further supports this observation.

Hence, it may be concluded that by choosing a suitable MO_x for the modification of γ -alumina, the desired redox property could be achieved which enhances the partial oxidation activity of the vanadia catalyst.

ACKNOWLEDGMENTS

LJL and STS thank the Council of Scientific and Industrial Research, New Delhi for the award of research associateships.

REFERENCES

1. Oyama, S.T. and Somorjai, G.A., *J. Phys. Chem.* **94**, 5022 (1990).
2. Deo, G. and Wachs, I.E., *J. Catal.* **146**, 325 (1994).
3. Owens, L. and Kung, H.H., *J. Catal.* **148**, 587 (1994).
4. Sobalik, Z., Markvart, M. and Lapina, O.B., *Catal. Lett.* **28**, 25 (1994).
5. Eon, J.G., Olier, R. and Volta, J.C., *J. Catal.* **145**, 318 (1994).
6. Weissmann, J.G., *Appl. Catal.* **94**, 45 (1993).
7. Shen, J., Cortright, R.D., Chen, Y. and Dumesic, J.A. *J. Phys. Chem.* **98**, 8067 (1994).
8. Shen, J., Cortright, R.D., Chen Y. and Dumesic, J.A., *Catal. Lett.* **26**, 247 (1994).
9. Trawlzynski, J. and Walendziewski, J., *Appl. Catal.* **119**, 59 (1994).
10. Lakshmi, L.J., Narsimha, K. and Kanta Rao, P., *Appl. Catal.* **94**, 61 (1993).
11. Corma, A., Fornes, V., Juan-Rajadell, M.I., and Lopez Nieto, J.M., *Appl. Catal.* **116**, 151 (1994).
12. Wei, Z., Xin, Q., Guo, X., Grange, P. and Delmon, B., *Appl. Catal.* **75**, 178 (1991).
13. Reddy, B.M., Narsimha, K., Sivaraj, Ch. and Kanta Rao, P., *Appl. Catal.* **55**, 1, (1991).
14. Nag, N.K., Chary, K.V.R., Reddy, B.M., Rama Rao, B. and Subrahmanyam, V.S., *Appl. Catal.* **9**, 225 (1984).
15. Bond, G.C., Flamerz, S. and Shukri, R., *Faraday, Discuss. Chem. Soc.* **87**, 65 (1989).

Table 1: Physico-chemical properties and the product distribution during the IPA decomposition on vanadia catalysts.

Catalyst	Surface area (m ² /g)	O ₂ uptake (μmol/g)	Surface coverage (%)	Active site density (nm ⁻²)	IPA conv. (%)	Acetone sel. (%)	Propylene sel. (%)
1. VAl	168	56	9.9	0.40	7	100	--
2. VTiAl	122	133	32.3	1.21	23	74	26
3. VZrAl	129	89	20.4	0.83	19	83	17
4. VLaAl	153	58	10.8	0.44	12	98	2
5. VMgAl	115	22	5.7	0.28	4	99	1

¹ Surface coverage is defined as 100x active surface area/BET SA of reduced catalyst.

² Active site density is the number of 'O' atoms chemisorbed per unit area of catalyst.

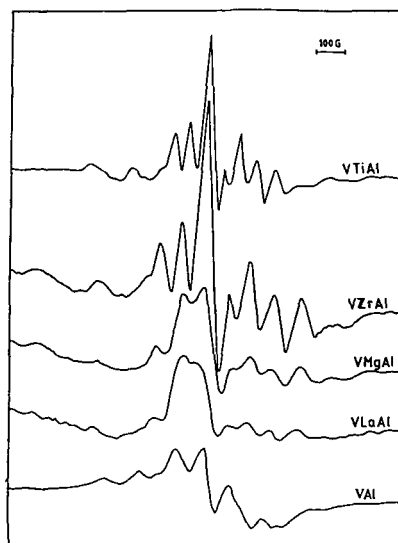


Figure 1. ESR patterns of the VAl and VMAl catalysts.

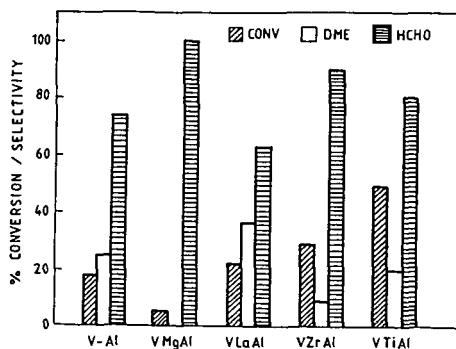


Figure 2. Methanol partial oxidation activity and selectivities on VAl and VMAl catalysts.

LIQUIDIZATION OF DEWATERED ORGANIC SLUDGE AND ANAEROBIC TREATMENT

Shigeki Sawayama, Seiichi Inoue, & Tomoko Ogi
*Biomass Laboratory, National Institute for Resources and Environment,
16-3 Onogawa, Tsukuba, Ibaraki, 305, Japan*

Keywords: Anaerobic digestion, Organic sludge, Thermochemical liquidization

ABSTRACT

Dewatered sewage sludge was thermochemically liquidized at 175 °C and the liquidized sludge was separated by centrifugation to 58% (w/w) supernatant and 42% precipitate. The amount of proteins in the liquidized sludge slightly decreased through the liquidization process, however, that of lipids increased. The supernatant separated from the sludge liquidized with dewatered sewage sludge was successfully anaerobically digested. Biogas yield from the supernatant from dewatered sewage sludge at organic loading concentrations of 1.9-2.2 g VS/l during 9 days' incubation was 440 ml/g-added VS and digestion ratio was 66% (w/w). Biogas yield in the case of dewatered sewage sludge was 257 ml/g-added VS and digestion ratio was 45%. Similar results were obtained in the case of the anaerobically digested with sewage sludge and dewatered sludge. Anaerobic digestion of the supernatants from the liquidized sludges resulted in high biogas productivity and high digestion ratio compared with these of the original sludges. Moreover, the precipitates contained lower moisture, therefore, they can be incinerated easier than the respective original sludges.

INTRODUCTION

Treatments of sewage sludge and anaerobically digested sludge have been important environmental issues to resolve. Anaerobic digestion of sewage sludge is commonly used for treatment of sewage sludge and energy is recovered in the form of methane (Fannin *et al.*, 1983). A thermal pretreatment system for anaerobic digestion of concentrated sewage sludge with 2-3% volatile solid (VS) has been studied to improve anaerobic digestibility and dewatering properties (Haug, 1977; Haug *et al.*, 1978; Haug *et al.*, 1983; Hiraoka *et al.*, 1984). The volume of concentrated sewage sludge for thermal pretreatment is huge, and therefore this process consumes a large amount of energy.

Dewatered sludges (VS of 12%) are clay like solids and are therefore not suitable for anaerobic digestion. An attempt at liquidization of dewatered sewage sludge by a thermochemical process was conducted (Dote *et al.*, 1993; Sawayama *et al.*, 1995). The volume of dewatered sewage sludge decreased markedly from that of concentrated sewage sludge (VS of 2-3%), suggesting that heat treatment of dewatered sewage sludge would require less energy than in the case of concentrated sewage sludge. As for anaerobically digested sludge, thermochemical liquidization can possibly improve anaerobic re-digestibility and the dewatering properties.

This paper deals with the thermochemical liquidization of dewatered sewage sludge and anaerobically digested and dewatered sludge, and the batch anaerobic digestion of the supernatants separated from the liquidized sludges.

METHODS

Liquidization of sludge

Dewatered sewage sludge, and anaerobically digested and dewatered sludge used in the experiment were obtained from an aerobic sewage treatment facility for domestic sewage in Ibaraki prefecture, Japan. The liquidization of the dewatered sludges were conducted as previously demonstrated (Dote *et al.*, 1993). After purging with nitrogen gas, the dewatered sludge was heated at 175°C in an electric furnace and held at 175°C for 1 h in a 1 l autoclave (4 MPa). The liquidized sludge was separated by centrifugation (1000 g, 10 min) to supernatant and precipitate.

Anaerobic digestion

Seed sludge for batch anaerobic digestion was obtained from the sewage sludge treatment facility in Ibaraki prefecture, Japan. Two liters of the seed sludge (VS concentration: approximately 1 %, w/w) was incubated in a 2 l conical flask at 35°C. A sample was added to the seed sludge at 1.6-2.2 g-VS/l and air in the digester was purged with nitrogen gas. Samples for anaerobic digestion included the original sludges (dewatered sewage sludge, and anaerobically digested and dewatered sludge), liquidized sludges and separated supernatants. The gas production yield from the digester was monitored by displacement of saturated sodium chloride solution.

Analyses of sludges and gas

Moisture content was determined by heating the sample at 105°C for 24 h before weighing, and VS and ash content were determined by heating at 600°C for 1 h. Digestion ratio was expressed as the ratio of the amount of VS decrease during 9 or 8 days' digestion to the amount of VS added.

The Kjeldahl-nitrogen method was used for protein analysis. After extraction, a gravimetric method was used for determination of lipids. The Somogyi method was used for carbohydrate analysis.

High heating value (HQ , MJ/kg) for VS of sludges is calculated using to Dulong's formula (Selvig & Gibson, 1945):

$$HQ = 0.3383 \times C + 1.442(H - O/8)$$

where C , H and O are weight percentages of carbon, hydrogen and oxygen, respectively. Low heating value (LQ , MJ/kg) is calculated using the following equation:

$$LQ = HQ \times V - 0.0251 \times (9 \times H + M)$$

where V is the ratio of volatile solid and M is the weight percentage of moisture.

The biogas composition was determined by gas chromatography. The digestion ratio was expressed as the ratio of decreased VS during 9 or 8 days of digestion versus added VS.

RESULTS AND DISCUSSION

Liquidization

Procedures of liquidization and anaerobic treatment for sewage sludge are shown in Fig. 1, and those of liquidization and anaerobic re-treatment for anaerobically digested and dewatered sludge are shown in Fig. 2. Dewatered sewage sludge (moisture, 84%, w/w; VS, 12%, w/w), and anaerobically digested and dewatered sludge (moisture; 84%, w/w, VS; 11%, w/w) were successfully liquidized by thermochemical reaction at 175°C with holding time of 1h. The protein content (33 %) in the sewage sludge was higher than that (28%) in the liquidized sludge. On the other hand, the lipid content (14%) in the liquidized sludge from the sewage sludge was approximately two times higher than that (7%) in the sewage sludge. It was reported that volatile acids would be produced through thermal treatment (170-230 °C) of sewage sludge (Fisher & Swanwick, 1971). These results suggest that proteins were converted to lipids through the liquidization process.

The liquidized sludge from the dewatered sewage sludge was separated by centrifugation to supernatant (58%, w/w) and precipitate (42%, w/w), and that from the anaerobically digested and dewatered sludge was separated to supernatant (46%, w/w) and precipitate (54%, w/w). The moisture content of the precipitates decreased from the both original sludges through centrifugation, therefore, thermal liquidization of organic sludges was considered to be a pretreatment for dewatering.

Anaerobic digestion

The supernatant separated from the sludge liquidized with the dewatered sewage sludge was successfully anaerobically digested. The digestion ratio (66%) of the supernatant was higher than that of the original sewage sludge (45%) after 9 days of incubation. The total biogas yield from the supernatant during 9 days' incubation was 440 ml /g-added VS (Fig. 3) and the total methane yield was 328 ml /g-added VS. The biogas productivity in the anaerobic treatment of the supernatant was improved by thermochemical treatment compared with those of the original sewage sludge and the liquidized sludge. There was no difference in methane contents of biogas (75-77%) among those three anaerobic experiments.

The digestion ratio (61%) of the supernatant from the sludge liquidized with the anaerobically digested and dewatered sludge was higher than that of the original sludge (27%) after 8 days of incubation. The total biogas yield from the supernatant after 8 days of incubation was 339 ml /g-added VS (Fig. 3) and the total methane yield was 253 ml /g-added VS. The biogas conversion ratio of the supernatant based on carbon was 36 %. The improvement in the digestion ratio of the anaerobically digested sludge by thermal pretreatment was more apparent than that of the sewage sludge. This effect was thought to be partly caused by degradation of the cell wall and membrane and to be the same effect caused by the thermal treatment of sewage sludge reported by Hauger *et al.*, 1978.

Anaerobic treatment of the thermal treatment liquor (average COD; 6-10 g/l) has been studied (Pugh *et al.*, 1987; Kimata *et al.*, 1993). After this preliminary batch experiment, application of the anaerobic digestion method with granular sludge such as the UASB method could contribute to a faster digestion rate for the supernatant from liquidized sludge.

Low heating values of precipitates

The precipitate separated from the sludge liquidized with the dewatered sewage sludge was composed of 71% moisture, 19% VS and 10% ash. The precipitate obtained by centrifugation of the sludge liquidized with the anaerobically digested and dewatered sludge was composed of 76% moisture, 14% VS and 10% ash. This thermochemical liquidization process improved the dewaterability of the dewatered sludges.

The calculated low heating value of the precipitate separated from the sludge liquidized with the dewatered sewage sludge was 1.2 MJ/kg and that of the original sludge was -1.0 MJ/kg. The calculated low heating value of the precipitate separated from the sludge liquidized with the anaerobically digested and dewatered sludge was -0.4 MJ/kg and that of the original sludge was -1.6 MJ/kg. The precipitates separated from the liquidized sludges have higher heating values compared to those of the original dewatered sludges which means that incineration of the precipitate could save energy by using less fuel. A more suitable dewatering method for liquidized sludges would provide higher low heating values for their solid fractions.

ACKNOWLEDGMENT

We are grateful to Wastewater Treatment Office in Ibaraki prefecture for preparation of the sewage sludge and to Dr. Yutaka Dote in Department of Civil and Environmental Engineering, Miyazaki University for the useful discussions.

REFERENCES

- Dote, Y., Yokoyama, S., Minowa, T., Masuta, T., Sato, K., Itoh, S. & Suzuki, A. (1993). Thermochemical liquidization of dewatered sewage sludge. *Biomass Bioenergy*, **4**, 243-248.
- Fannin, K. F., Conrad, J. R., Srivastava, V. J., Jerger, D. E. & Chynoweth, D. P. (1983). Anaerobic processes. *J. Water Poll. Control Fed.*, **55**, 623-632.
- Fisher, W. J. & Swanwick, J. D. (1971). High-temperature treatment of sewage sludges. *Water Poll. Control*, **70**, 355-373.
- Haug, R. T. (1977). Sludge processing to optimize digestibility and energy production. *J. Water Poll. Control Fed.*, **49**, 1713-1721.
- Haug, R.T., Stuckey, D.C., Gossett, J.M., and McCarty, P.L. (1978). Effect of thermal pretreatment on digestibility and dewaterability of organic sludges. *J. Water Poll. Control Fed.*, **50**, 73-85.
- Haug, R.T., LeBrun, T.J., and Tortorici, L.D. (1983). Thermal pretreatment of sludges - a field demonstration. *J. Water Poll. Control Fed.*, **55**, 23-34.
- Hiraoka, M., Takeda, N., Sakai, S., and Yasuda, A.: Highly efficient anaerobic digestion with thermal pretreatment. *Water Sci. Technol.*, **17**, 529-539 (1984).
- Kimata, T., Kawai, T., Tada, M., Tanaka, K., Shinabe, K. & Shimizu, K. (1993). Anaerobic treatment of thermal sludge conditioning liquor with granular sludge. *Water Environ. Res.*, **65**, 6-14.
- Pugh, L. B., Kang S. J. & Spangler, J. L. (1987). Anaerobic fluidized bed and anaerobic filter/contact stabilization application for heat treatment liquor. *J. Water Poll. Control Fed.*, **59**, 1050-1058.
- Sawayama, S., Inoue, S., Yagishita, T., Ogi, T. & Yokoyama, S. (1995). Thermochemical liquidization and anaerobic treatment of dewatered sewage sludge. *J. Ferment. Bioeng.*, **79**, 300-302.
- Selvig, W. A. & Gibson, F. H. (1945). Calorific value of coal. In *Chemistry of Coal Utilization*. ed. H. H. Lowry. John Wiley & Sons, New York, pp. 132-144.

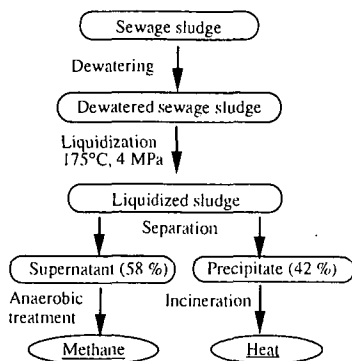


Fig. 1. Flow diagram of liquidization and anaerobic treatment of sewage sludge.

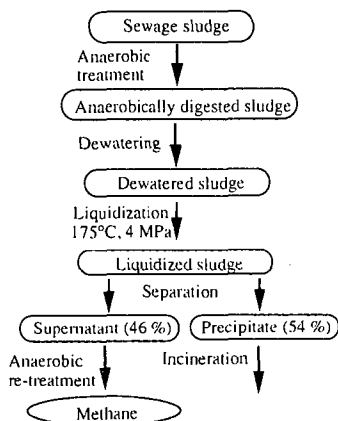


Fig. 2. Flow diagram of liquidization and anaerobic re-treatment of anaerobically digested sludge

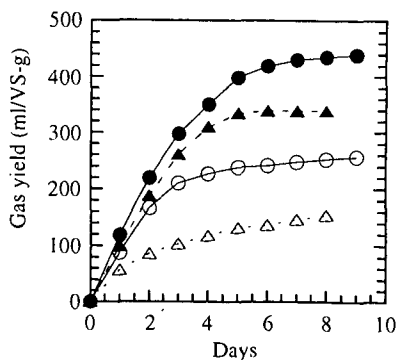


Fig. 3. Gas yield from anaerobic treatments from sewage sludge (open circle) and anaerobically digested sludge (open triangle), and supernatant (closed circle) from sewage sludge and supernatant (closed triangle) from anaerobically digested sludge.

IGNITABILITY OF VARIOUS COALS AS MEASURED BY LASER IGNITION

John C. Chen,[†] Subrahmanyam Musti,^{*} Vinayak Kabadi^{*}

Departments of [†]Mechanical and ^{*}Chemical Engineering
North Carolina A&T State University
Greensboro, NC 27411

KEYWORDS: Coal ignition, laser, coal reactivity

INTRODUCTION

We present a novel experiment designed to study the ignition and combustion of pulverized fuels in a room-temperature gas environment. The absence of hot furnace walls surrounding the test section allowed for optical detection of the reaction sequence. Our goals are to determine, by direct observation, the ignition mechanism (heterogeneous or homogeneous ignition) of a range of coals, and to quantify the differences in ignition reactivity between the fuels.

EXPERIMENT

The experiment is similar to one described in detail elsewhere,¹ so only a brief description is given here. Figure 1 presents a schematic of the laser ignition experiment; the inset shows the details around the test section. Sieve-sized particles were dropped through a tube into a laminar, upward-flow wind tunnel with a quartz test section (5 cm square cross-section). The gas was not preheated. The gas flow rate was set so that the particles emerged from the feeder tube, fell approximately 5 cm, then turned and traveled upward out of the tunnel. This ensured that the particles were moving slowly downward at the ignition point, chosen to be 2 cm below the feeder-tube exit. A single pulse from a Nd:YAG laser was focused through the test section, then defocused after exiting the test section, and two addition prisms folded the beam back through the ignition point. Heating the particles from two sides in this manner achieved more spatial uniformity and allowed for higher energy input than a single laser pass. For nearly every case, two to five particles were contained in the volume formed by the two intersecting beams, as determined by previous observation with high-speed video.²

The laser operated at 10 Hz and emitted a nearly collimated beam (6 mm diameter) in the near-infrared (1.06 μm wavelength). The laser pulse duration was $\sim 100 \mu\text{s}$ and the pulse energy was fixed at 830 mJ per pulse, with pulse-to-pulse energy fluctuations of less than 3%. The laser pulse energy delivered to the test section was varied by a polarizer placed after the laser exit; variation from 150 to 750 mJ was achieved by rotating the polarizer. Increases in the laser pulse energy result in heating of the coal particles to higher temperatures. At the ignition point the beam diameter normal to its propagation direction was $\sim 3 \text{ mm}$ on each pass of the beam. An air-piston-driven laser gate (see Fig. 1) permitted the passage of a single pulse to the test section. The system allowed for control of the delay time between the firing of feeder and the passage of the laser pulse. Finally, ignition or nonignition was determined by examining the signal generated by a high-speed silicon photodiode connected to a digital oscilloscope, as described elsewhere.¹

We report here the ignition behavior of four coals ranging in rank from subbituminous to medium-volatile bituminous. All samples were obtained from the Penn State University Coal Sample Bank, and the reported proximate and ultimate analyses are shown in Table 1. The coals were sieve-sized using a Ro-Tap shaker to $-120/+140$ mesh (106-125 μm diameter), and dried at 70°C under vacuum for at least 12 hours prior to each day's experiment.

RESULTS

Each day's experiment was conducted as follows: After choosing the coal and oxygen concentration to examine, the coal was loaded into the batch-wise feeder. The delay time between the triggering of the feeder and the appearance of the coal batch at the feeder tube exit was measured by visual observation in conjunction with a stop watch; typical values were $\sim 2.9 \text{ s}$. The delay time was then programmed into the device which triggered the laser gate. The gas flow rate needed to achieve a drop distance of $\sim 5 \text{ cm}$ for the coal batch was also determined by visual observation. Finally, a laser pulse energy was chosen, and the experiment commenced. At each set of operating conditions (coal type and size, oxygen concentration, and laser energy), 20 attempts at ignition were made in order to measure the ignition frequency, or probability, which is the parameter sought from these studies. Mapping this ignition frequency over a range of laser pulse energy produces an ignition-frequency distribution.

Such a frequency distribution is shown in Fig. 2 for the Pittsburgh #8 coal. It can be seen that at each oxygen concentration, ignition frequency increases monotonically over a range of increasing laser pulse energy. Below this range the ignition frequency is zero, and higher energies result in 100% ignition frequency. This behavior is due to the fact that, within any coal sample, there exists a variation of reactivity among the particles.³ Thus, in this experiment, in which a batch of perhaps several hundred particles of a sample is dropped into the test section but only a few are heated by the laser pulse, there is an increasing probability (or frequency) as the laser energy is increased that at least one of the heated particles is reactive enough to ignite under the given conditions.

The repeated distributions under 100% oxygen, measured on separate days, show the excellent repeatability of this experiment; the most important factor for reproducibility is the moisture content of the sample.

Figure 2 also shows the effect of oxygen concentration: As oxygen level is decreased from 100% to 75%, and then to 50%, the frequency distribution shifts to higher laser energies or, equivalently, higher particles temperatures, as expected. This is consistent with ignition theory since at decreased oxygen levels, higher temperatures are necessary to achieve the equality between heat generation by the particles (due to chemical reactions) and heat loss from the particles. This equality is the minimum requirement for ignition, and is termed 'critical ignition.' The shift in distribution can be viewed in two ways: First, for a fixed laser pulse energy, a decrease in oxygen level leads to a decrease in the ignition frequency, all else being the same; second, a decrease in oxygen implies that a higher laser pulse energy is needed, in order to achieve the same ignition frequency.

Finally, it should be noted that for the Pittsburgh #8, the decreases in oxygen concentration shift the distributions to higher laser energies in approximately equal increments (equal energy ranges), and with little or no effect on the slope of the distributions. This finding is in contrast to the results for the Sewell coal (Fig. 3).

Three major differences between the ignition behaviors of the Pittsburgh #8 and Sewell exist. First, decreasing oxygen concentrations has a stronger effect in shifting the distributions of the Sewell to higher laser pulse energies (or higher particle temperatures). Second, as oxygen level is decreased, the slope of the distribution is undoubtedly decreased for the Sewell, while little effect is observed for the Pittsburgh #8. Finally, a comparison of the distributions of the two coals under 100% oxygen shows that the Sewell reaches 100% ignition frequency in a significantly smaller range of laser energy (~150 mJ versus ~250 mJ).

The results for the two remaining coals — the Illinois #6 and the Wyodak — are shown in Figs. 4 and 5. The two coals span similar ranges in going from 0 to 100% ignition frequency (~350 mJ), which are larger than both the Pittsburgh #8 or Sewell coals. Comparing the results for these two coals, it is also observed that the ignition-frequency distributions of the Illinois #6 are shifted to higher laser energies than the Wyodak, implying that the Illinois #6 is a less reactive coal, at least with regard to ignition.

DISCUSSION

Over the past three decades, many experiments have examined the ignition of pulverized coals under conditions which simulate pulverized fuel-firing conditions.^{4,5,6,7,8,9} The common factor among these studies is the assumption of a single, average, kinetic rate-constant in describing the ignition reactivity of each coal. As we have shown previously,³ it is necessary to account for the variation in reactivity among the particles within a sample in order to model the ignition distribution observed in this and nearly all previous ignition studies. Once such a model is implemented, the parameters may then be adjusted to fit the data and produce the desired ignition rate constant and reaction order with respect to oxygen for each coal.

Our previous experience in modeling ignition distribution data³ provides some insight to explain the results described earlier. The model details will not be described here, but it is sufficient to note that the model accounts for particle-to-particle variations in reactivity by having a single preexponential factor and a Gaussian distribution of activation energies among the particles within a sample.

In light of this model, the differences in the range of laser energies over which the various coals achieved 100% ignition frequency is a direct result of the breadth of the Gaussian distribution of activation energies: A narrow distribution (small standard deviation) leads to a small laser-energy range since most particles have similar activation energies and, thus, reactivities. Indeed, in the limit that the standard deviation is zero (all particles have the same

activation energy), the ignition-frequency distribution would become a step function. Conversely, a broad distribution of reactivities leads to a relatively larger range of laser energy needed to achieve 100% frequency, as is the case for the Pittsburgh #8 compared to the Sewell. The fact that the Illinois #6 and Wyodak coals span a similar laser-energy range suggests that the spread of their reactivity distributions are similar. However, since the ignition-frequency distributions of the Illinois #6 are shifted to higher laser energies than the Wyodak, the interpretation is that the reactivity distribution of the Illinois #6 has a lower average activation energy, and therefore it is more reactive, as stated earlier.

Finally, with regard to the effect of oxygen concentration on the slope and shift of the ignition-frequency distributions observed for the Pittsburgh #8 and Sewell coals, the model interprets such differences to be the result of the variation in the reaction order with respect to oxygen concentration. We are presently at work on modeling the results reported here, with the goal of presenting kinetic rate parameters in the near future.

ACKNOWLEDGEMENT

The support of this project by the U.S. Department of Energy through Grant DE-FG22-94MT94012 is gratefully acknowledged. The assistance of Cynthia Marshall and Monique Jenkins with the experiments is also greatly appreciated.

REFERENCES

- 1 Chen, J.C., Taniguchi, M., Narato, K., and Ito, K. "Laser Ignition of Pulverized Coal," *Combust. Flame* 97, 107 (1994).
- 2 Chen, J.C., Taniguchi, M., Ito, K. "Observation of Laser Ignition and Combustion of Pulverized Coals," *Fuel*, 74(3), 323 (1995).
- 3 Chen, J. C. "Distributed Activation Energy Model of Heterogeneous Coal Ignition," *Combust. Flame*, in press (1996).
- 4 Essenhigh, R.H., Mahendra, K.M., and Shaw, D.W. *Combust. Flame*, 77, 3 (1989).
- 5 Cassel, H.M. and Liebman, I. *Combust. Flame*, 3, 467 (1959).
- 6 Karcz, H., Kordylewski, W., and Rybak, W. *Fuel*, 59, 799 (1980).
- 7 Fu, W. and Zeng, T. *Combust. Flame*, 88, 413 (1992).
- 8 Zhang, D., Wall, T.F., Harrie, D.J., Smith, I.W., Chen, J., and Stanmore, B.R. *Fuel*, 71, 1239 (1992).
- 9 Boukara, R., Gadiou, R., Gilot, P., Delfosse, L., and Prado, G. *Twenty-Fourth Symposium (International) on Combustion*, The Combustion Institute, Pittsburgh, PA, 1993, pp. 1127-1133.

Coal Penn State ID	Rank	Prox. Analy. (dry wt%)		Ultimate Analysis (dry, ash-free wt%)				
		Vol. Matter	Ash	C	H	N	S	O (diff.)
Pittsburgh #8 (DECS 23)	low-volatile A bituminous	39.4	9.44	82.0	5.63	1.49	4.27	6.66
Sewell (DECS 13)	medium-volatile bituminous	25.0	4.22	88.2	4.95	1.50	0.65	4.71
Illinois #6 (DECS 24)	high-volatile C bituminous	40.8	13.4	76.3	5.30	1.32	6.38	10.74
Wyodak (DECS 26)	subbituminous B	44.9	7.57	75.5	6.11	1.02	0.47	16.92

Table 1: Ultimate and proximate analyses of coals used in this study.

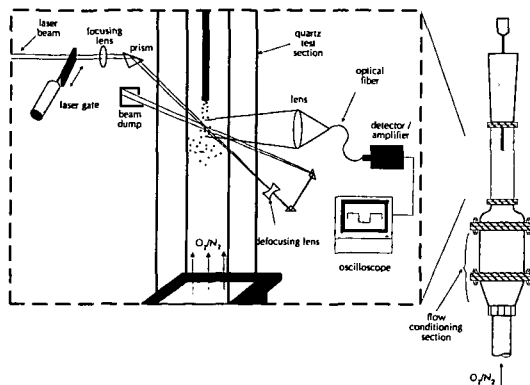


Fig. 1: Schematic of the laser ignition experiment.

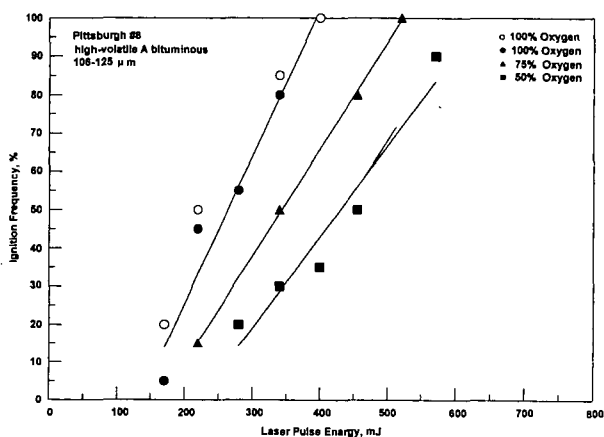


Fig. 2: Ignition-frequency distributions for the Pittsburgh #8 coal. Two data sets (open and filled circles) at 100% oxygen show reproducibility of experiment.

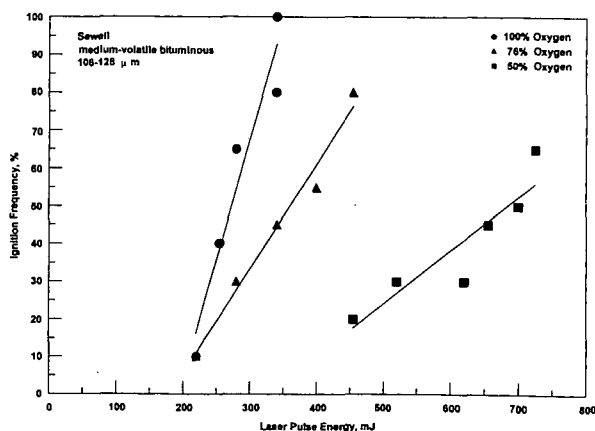


Fig. 3: Ignition-frequency distributions for the Sewell coal.

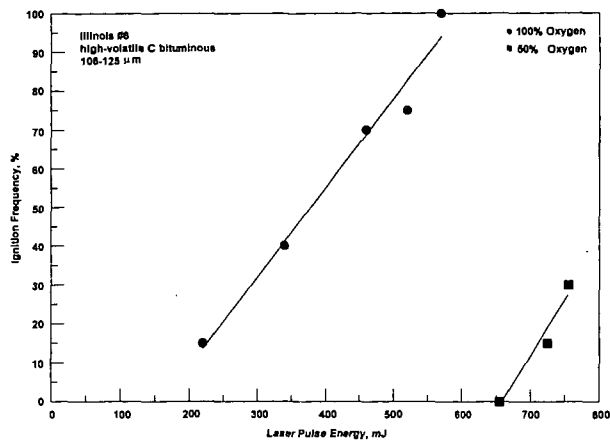


Fig. 4: Ignition-frequency distributions for the Illinois #6 coal.

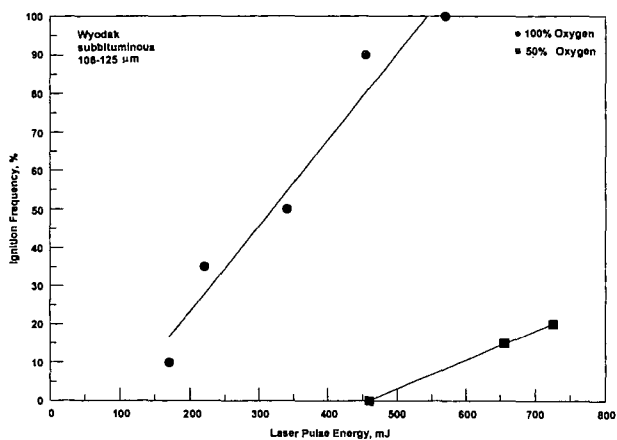


Fig. 5: Ignition-frequency distributions for the Wyodak coal.

MODELING OF SMOLDERING CELLULOSIC MATERIALS- EVAPORATION AND PYROLYSIS PROCESSES

Sung-Chul Yi and Young Chai Kim

Department of Chemical Engineering, Hanyang University, 17, Haengdang-dong,
Sungdong-ku, Seoul, 133-791, Korea

Keywords: model, smoldering, cellulosic material

INTRODUCTION

Over 1600 people die each year [Miller, 1991] from fires started by smoking materials (cigarettes, matches, etc.), and many times that number are hurt and/or disfigured; most of those fires are established in upholstered furniture. As a result, Congress passed the Cigarette Safety Act of 1984. One of the tasks under the Act was to model mathematically the behavior of upholstered furniture and the cigarette, when a smoldering cigarette is dropped onto it. To do this, the heating of the substrate when subjected to a moving heat source must first be accurately modeled, and a criterion established for its ignition. In order to examine how changing one or more properties of the cigarette will influence its ignition propensity, it is also necessary to understand the behavior of a smoldering cigarette. This includes knowing how its external heat flux and burning velocity depend upon its physical and/or chemical properties.

Considerable effort has been expended in the study of the burning cellulosic material such as tobacco etc.. Egerton et al. [1963] studied the smoldering combustion in cigarettes. From the data of various experiments, they explained several aspects of the mechanism of smoldering. A theoretical and experimental investigation of the smoldering mechanism of a cylindrical cellulosic rod was carried out by Moussa et al. [1976]. They proposed a simple steady-state, 1-dimensional model of a burning cellulosic rod. Based on a postulated mechanism of smoldering, Muramatsu et al. [1979] developed one-dimensional model of the pyrolysis/distillation zone. Their model contains four general pyrolysis reactions, one distillation process and combined conductive and radiative heat transfer from the combustion zone.

The purpose of this paper is to present the results of a study using numerical techniques to compute the static burn rate, mass burn rate, heat flux and the amount of heat released in the natural smoldering cigarette. The study was made on cigarettes containing flue-cured and burley tobaccos since physical properties and kinetic data are readily available [Muramatsu et al. 1979].

MATHEMATICAL MODEL

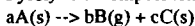
A cigarette generally includes a filter attached to the end of the tobacco rod. The rod is a packed column of approximately 1 g of shredded tobacco, generally 8 mm in diameter and 70 mm long, wrapped in a thin porous paper. The shreds are nonuniformly packed in the tobacco rod which contains about 70 - 85 % void space.

Smoldering is a non-flaming combustion mode, characterized by thermal degradation and charring of the virgin tobacco, evolution of smoke, and emission of a visible glow. The temperature in the burning zone increases to the ignition temperature, and the temperature gradients are directly correlated to the basic processes which take place in the cigarette (i.e. distillation, pyrolysis, and combustion) and affect the absolute density [Baker, 1979] of the rod in the burning zone.

During natural burning the oxygen transport to the surface is restricted and the peripheral region with its large heat losses cannot maintain rapid surface oxidation. Muramatsu et al. have developed a model of the evaporation-pyrolysis processes with the following assumptions:

- 1) The solid phase and the gas phase inside the burning tobacco are the same temperature.
- 2) Heat loss from the outer surface of the element is caused by free convection and radiation.
- 3) Heat transfer inside the cigarette column is caused by thermal conduction characterized by a effective thermal conductivity.

Pyrolytic decomposition of tobacco can be expressed by the following simplified equation;



The virgin tobacco and its water content are gradually consumed to form smoke, water vapor, and a residual char with final density ρ_r . In the steady state of combustion, the temperature is raised by the heat transferred from the burning zone. The temperature distribution of the tobacco column depends upon the thermal properties of the cigarette such as the effective thermal conductivity, specific heat and thermal diffusivity. The total density of the burning tobacco is given by

$$\rho_t = \rho_v + \rho_g + \rho_r \quad (1)$$

where ρ is density, and the subscripts t, v, c, and w stand for total, unreacted tobacco, carbonaceous residue, and water, respectively. The conversion of virgin tobacco can be expressed by

$$\frac{\partial \rho_v}{\partial t} = \sum_{i=1}^4 \frac{\partial \rho_{vi}}{\partial t} \quad (2)$$

and then the individual Arrhenius forms:

$$\frac{\partial \rho_{vi}}{\partial t} = -A_i \exp\left(\frac{-E_i}{RT}\right) \left(\frac{\rho_{vi}}{\rho_{vi}^o}\right)^n \rho_{vi}^o \quad (3)$$

and the char density is given by

$$\frac{\partial \rho_c}{\partial t} = - \sum_{i=1}^4 \frac{\rho_f}{\rho_{vi}^o} \frac{\partial \rho_{vi}}{\partial t} \quad (4)$$

where superscript o is the initial state. The loss of tobacco moisture from a tobacco rod is assumed to involve both the conversion of moisture to a water vapor as well as mass transfer of the moisture out of the tobacco rod. The evaporation rate of the water from tobacco can be expressed by the empirical equation,

$$\frac{\partial w}{\partial t} = - \left(\frac{S}{w}\right) \exp\left(\frac{-\theta}{T}\right) (w - w_{eq})^\beta \quad (5)$$

where w is water content in tobacco, S is surface area of a tobacco lamina, θ and β are empirical constants, and subscript eq is equilibrium state. The pyrolysis reaction of virgin tobacco in the region where water evaporation takes place is slow, and can be considered to be negligible. Thus

$$\frac{\partial \rho_w}{\partial t} = -N_s \alpha \exp\left(\frac{-\theta}{T}\right) (w - w_{eq})^\beta = \sum_{i=1}^4 \rho_{vi}^o \frac{\partial w}{\partial t} \quad (6)$$

where N_s is total surface area of tobacco shreds per unit volume of a cigarette, α is experimental constant, and w_{eq} is related to the water vapor pressure, p_w , by

$$w_{eq} = \frac{p_w / p_{ws}}{a + b \left(\frac{p_w}{p_{ws}} \right) - c \left(\frac{p_w}{p_{ws}} \right)^2} \quad (7)$$

The saturated vapor pressure of water, p_{ws} , can be expressed by Calingart's equation [Calingart and Davis, 1925] as follows;

$$\log p_{ws} = 7.991 - \frac{1687}{T - 43} \quad (8)$$

The mass balance equation for the water vapor pressure, p_w , inside the tobacco rod is

$$\frac{\partial}{\partial t} \left(\frac{p_w}{RT} \right) = \frac{\partial}{\partial z} \left\{ D_s \frac{\partial}{\partial z} \left(\frac{p_w}{RT} \right) \right\} - \frac{2D_r}{\Phi r \delta RT} \left(p_w - p_{ws} \frac{T}{T_\infty} \right) - \frac{\sum_{i=1}^4 \rho_{vi}^o}{\Phi m} \frac{\partial w}{\partial t} \quad (9)$$

where the first term of left hand side is the net rate of accumulation of water vapor, the first term of right hand side (rhs) is the rate of accumulation water vapor by diffusion, the second term of rhs is the rate of loss of water vapor by diffusion through a cigarette paper of thickness, δ , and the last term is the rate of evaporation of water from the tobacco.

The heat balance equation for the element is given by

$$\frac{\partial (H_v \rho_v + H_c \rho_c + H_w \rho_w)}{\partial t} = \frac{\partial}{\partial z} \left(K_r \frac{\partial T}{\partial z} \right) + Q_p \frac{\partial \rho_v}{\partial t} + Q_w \frac{\partial \rho_w}{\partial t} - \frac{2}{r} \{ h(T - T_\infty) + \sigma \epsilon_r (T^4 - T_\infty^4) \} \quad (10)$$

where the thermal conductivity, K_r , depends upon the void fraction, ϕ and the temperature, T .

$$K_r = (1 - \phi^{2/3}) K_s + \phi^{1/3} \left(1 + \frac{2}{3} h_r D_p / K_s \right) K_s \quad (11)$$

where

$$h_r = 5.422 \times 10^{-12} \epsilon_r T^3$$

The cigarette weight after t time is;

$$M(t) = \pi r^2 \int_0^t \rho_s(t, r, \% \text{moisture}, \dots) dt \quad (12)$$

The heat flux is then given by;

$$q = \frac{1}{x} \int_0^x \frac{2}{r} [h(T - T_\infty) + \sigma \epsilon_r (T^4 - T_\infty^4)] dx \quad (13)$$

and the initial and boundary conditions are;

$$T = T_{\infty} @ x = -\infty$$

$$T = T_{\infty} @ x = x_o$$

$$\left(\frac{dT}{dx} \right)_{x=x_o} = \frac{u}{K_r} (T - T_{\infty}) (\rho_{1o} C_{p1o} + \rho_{wo} C_{pwo}) \quad (14)$$

$$\rho_{ao} = \frac{M_o}{V}, \rho_{wo} = \rho_{ao} \frac{w_o}{1 + w_o}, \rho_{ro} = 0.0, \rho_{vo} = \rho_{ao} - \rho_{wo}$$

w_o refers to the moisture content in the tobacco. The values of physical parameters used to solve the simultaneous differential equations can be obtained elsewhere [Muramatsu et al., 1979]. Then, the set of simultaneous differential equations can be solved numerically by the LSODE.

RESULTS AND DISCUSSIONS

In this section, we examine the factors affecting the static burn rate, the mass burn rate, heat flux and the heat released at the boundary by convection and radiation. The results are expected to provide a tool for understanding the mechanism of smoldering and controlling the physical parameters in the design of cigarette.

The mass burn rate (MBR), static burn rate (SBR), heat flux and heat released shown in Table 1 as a function of cigarette moisture at constant circumference and initial density. The analysis reveals that the SBR and MBR decrease with increased cigarette moisture content and are linear functions within the range of 10 to 15 % moisture. Thus, increased moisture reduces the rate of combustion due to the extra heat needed to vaporize water from the tobacco. The approximate value of heat flux regardless of moisture content are 0.327 and 0.177 cal/cm² sec for burley and flue-cured, respectively. The total heat released from the cigarette rod, neglecting the contribution from the paper is a function of the moisture content of the rod. The calculated heat released values at 12 % moisture are 1734 cal for burley and 1344 cal for flue-cured tobaccos. These values agree well with the results of Muramatsu et al.[1979]. Therefore, an increase in the tobacco moisture content causes a decrease in the static burn rate, but an increase in the total heat released.

The packing density of the cigarette has an effect on the SBR and MBR. Table 2 shows the typical smoldering speed calculated for a cigarette containing burley and flue-cured tobaccos and indicate that increasing the density at constant moisture and circumference causes the SBR to decrease. However, results show that the increase of the rod density appears to increase the MBR only slightly.

Table 3 summarizes the effect of rod circumference on the SBR and MBR. The results show that the MBR increase as circumference increases.

CONCLUSIONS

A mathematical model of the natural smoldering of cellulosic material is presented. The following conclusions can be drawn;

- 1) A simple interpretation of the calculation is that the variations in tobacco moisture content, rod density and circumferences can explain variations in SBR, MBR, heat flux and total heat released.
- 2) The calculation illustrates that the circumference of the cigarette is the major physical factor affecting MBR, while rod density strongly affects the SBR, heat flux, and heat released.
- 3) A quantitative relationship between these parameters and the MBR, SBR, and heat flux has been developed. The results may be a useful predictive tool for use in cigarette design.

REFERENCES

- Miller, A.L., NFPA Journal, Jan/Feb 86, (1991).
 Egerton, A., Gagan, K., and Weinberg, F.J., Combust. Flame 7:63 (1963).
 Moussa, N.A., Toong, T.Y., and Darris, C.A., Sixteenth Symposium (International) on Combustion, The Combustion Institute, Pittsburgh, 1447 (1977).
 Muramatsu, M., S. Umemura, and T. Okada, Combust. Flame 36:245 (1979).
 Baker, R.R., Thermochim Acta, 28 (1979).
 Calingert, G., and Davis, D.S., Ind. Eng. Chem. 17:1287 (1925).

Table 1. Calculated values of moisture content vs. SBR, MBR, and heat released.

A. Burley

Moisture content (%)	Static burn rate (10^{-3} cm/sec)	Mass burn rate (mg/min)	Heat released (cal)
10.0	6.497	74.178	1644.1
10.9	6.330	72.001	1691.7
12.0	6.112	69.218	1734.5
13.0	5.905	66.590	1797.4
14.0	5.692	63.951	1865.2
15.0	5.479	61.311	1937.6

B. Flue-cured

Moisture content (%)	Static burn rate (10^{-3} cm/sec)	Mass burn rate (mg/min)	Heat released (cal)
11.0	4.676	60.365	1308.7
12.0	4.563	58.731	1344.4
13.1	4.430	56.813	1387.9
14.0	4.318	55.220	1425.8
15.0	4.190	53.406	1471.1
16.0	4.060	51.587	1519.3

Table 2. Initial density effect on the SBR, MBR, and heat released.

Initial density (g/cc)	Static burn rate (10^{-3} cm/sec)		Mass burn rate (mg/min)		Heat released (cal)	
	flue-cured	burley	flue-cured	burley	flue-cured	burley
0.213	5.901	7.630	52.270	67.933	1057.2	1424.5
0.228	5.520	7.142	53.459	69.479	1133.3	1489.4
0.313	3.970	5.149	58.149	75.548	1552.9	2053.0
0.341	3.620	4.709	59.143	76.845	1693.5	2242.0
0.370	3.340	4.338	59.981	77.924	1838.4	2431.2

Table 3. Circumference effect on the MBR and heat released.

Circumference (cm)	Mass burn rate (mg/min)		Heat released (cal)	
	flue-cured	burley	flue-cured	burley
2.10	35.888	46.197	1563.6	1788.3
2.20	40.544	51.886	1511.8	1758.0
2.30	45.468	58.011	1466.8	1711.9
2.40	50.662	64.401	1431.3	1702.8
2.512	56.813	72.001	1387.9	1691.7
2.60	61.867	78.244	1371.2	1662.2
2.70	67.868	85.669	1363.4	1656.2
2.80	74.129	93.420	1344.6	1637.9

AN ANALYSIS OF COAL PYROLYSIS RATES USING THERMOGRAVIMETRY

Atsushi Inaba
National Institute for Resources and Environment
Tsukuba 305, JAPAN

Hiroyasu Okuo and Toshinori Kojima
Seikei University
Tokyo 113, JAPAN

INTRODUCTION

The modeling of coal pyrolysis reactions has been pursued since the initial studies by Gavalas and Howard. Recently, a large number of models has been reported, such as the FG-VDC, CPD, Flashchain and DEAM models. In these models, the activation energy or their distribution plays an important role.

In this study, the weight loss of coals by thermogravimetry (TG) was analyzed to obtain pyrolysis activation energies and frequency factors.

EXPERIMENTAL

Miike, Akabira, and Taiheiyo coals pulverized by a mortar and pestle were used in this study. The results of ultimate and proximate analyses are shown in Table 1.

Pyrolysis was carried out in nitrogen at atmospheric pressure (100 cc/min flow rate) or under vacuum conditions (10-30 Pa total pressure) using a TG to temperatures up to 1073 K at heating rates between 3 K/min and 100 K/min.

RESULTS

Figures 1 and 2 show the weight loss curves for Miike coal at atmospheric pressure and under vacuum, respectively. In both cases, the weight loss curve was moved to the higher temperature zone as the heating rate increases. This phenomenon is also seen in the degradation of synthetic polymers having the simple chemical bonds, such as polyethylene and polypropylene.

The final weight loss of coals heated to 1073 K under vacuum was larger than those under atmospheric pressure, suggesting that mass transfer strongly influences weight loss in experiments under atmospheric pressure.

ANALYSIS

Coal pyrolysis is generally analyzed as a first order reaction of volatile matter in the coal residue. In this study, the final weight loss at 1073 K under vacuum conditions, 0.58, 0.52, and 0.55 for Miike, Akabira, and Taiheiyo coals, respectively, was defined as the quantity of original volatile matter in the raw coals. These values were also used to model the experiments at atmospheric pressure.

Assuming a first order reaction and the Arrhenius Equation for the rate constant, Equation 1 is obtained.

$$(dV/dT)C = (A) \exp(-E/RT)(V^*-V) \quad (1)$$

where, A is frequency factor, E is activation energy, C is the heating rate, T is the temperature, and V* is the original volatile matter in the raw coal.

By integration of Equation 1, Equation 2 is obtained.

$$\ln(C/T^2) = -(E/R)(1/T) + \ln[(AR/E)/\ln(V^*/(V^*-V))] \quad (2)$$

Assuming that the rate constant, K, of the first order reaction is identical at the same extent of conversion at different heating rates, E at a specific extent of conversion can be obtained by plotting $\ln(C/T^2)$ vs. $(1/T)$, where T is the temperature at which the same conversion is obtained at each heating rate. A is then calculated using Equation 2.

Figure 3 shows the plot of $\ln(C/T^2)$ vs. $(1/T)$ of Miike coal pyrolyzed at atmospheric pressure for conversions from 0.2 to 0.6. Activation energies and frequency factors for the different conversions obtained by the above method are shown in Figures 4 and 5.

Figure 6 shows the relationship between A and E obtained for conversions between 0.2 and 0.6, which can be expressed as a line independent of coal and pressure. The rate constant of the first order reaction is defined by the combination of A and E. This suggests that coal degradation rate constant is the same for the conversions of 0.2 - 0.6 regardless of coals and pressure.

If the frequency factor is assumed to be constant during pyrolysis, a distribution of activation energies is obtained by Equation 3, which is a popular method for the analysis of the first order parallel reactions. In this study, the minimum frequency factors obtained by Figure 5 for the experiments under vacuum condition, which are 1.0×10^{12} , 1.5×10^{12} , $4.0 \times 10^{17} \text{ sec}^{-1}$ for Miike coal, Akabira coal and Taiheiyo coal respectively, are used. Figure 7 shows the distribution of the activation energy of each coal.

$$E = (RT) \ln[A(V^* - V)/(dV/dT)] \quad (3)$$

These figures show that activation energies for the experiments at atmospheric pressure and under vacuum are almost identical up to the approximately 0.6 conversion for each coal. On the other hand, activation energies for conversions greater than 0.6 are different at atmospheric pressure and under vacuum conditions. It suggests that the reaction at atmospheric pressure is controlled by mass transfer of the remaining heavy materials produced at conversion below approximately 0.6. It is essential to understand the chemistry of remaining materials in the coals in the experiments at atmospheric pressure.

REFERENCES

1. Gavalas, G.R., P.H.-K. Cheng, and R. Jain: Ind. Eng. Chem. Fundam., 20, 113-112 (1981).
2. Gavalas, G.R., R. Jan, and P.H.,-K Chen: *ibid.*, 20, 122-132 (1981).
3. Anthony, D.B. and J.B. Howard: AlChE J., 22, 625-656 (1976).
4. Howard, J.B.: "Chemistry of Coal Utilization", 2nd Suppl. p. 729 (1981).
5. Serio, M.A., D.G. Hambleton, and P.R. Solomon: Energy & Fuels, 1, 138-152 (1987).
6. Solomon, P.R., D.G. Hambleton, R.M. Carangelo, M.A. Serio, and G.V. Deshpande: *ibid.* 2, 405-422 (1988).
7. Fletcher, T.H., A.R. Kerstein, R.J. Pugmire, and D.M. Grant: Energy & Fuels, 4, 54-60 (1990).
8. Grant, D.M., R.J. Pugmire, T.H. Fletcher, and A.R. Kerstein: *ibid.*, 3, 175-186 (1989).
9. Niksa, S and A.R. Kerstein: *ibid.*, 5, 647-665 (1991).
10. Niksa, S.: *ibid.*, 5, 665-673 (1991).
11. Niksa, S.: *ibid.*, 5, 673-683 (1991).
12. Niksa, S. And C.-W. Law: Combustion and Flame, 94, 293-297 (1993).

Table 1. Analyses of Coals Used

Coal	Ultimate Analysis (daf st%)				Proximate Analysis (dry wt%)			
	C	H	N	S+O(diff.)	V.M.	F.C.	Ash	Water
Taikeiyo	74.87	6.55	0.89	17.69	45.87	43.71	10.42	1.24
Akabira	83.32	6.36	1.40	8.92	40.18	52.92	6.90	0.61
Miike	83.78	6.75	1.01	8.46	44.06	47.23	8.71	0.27

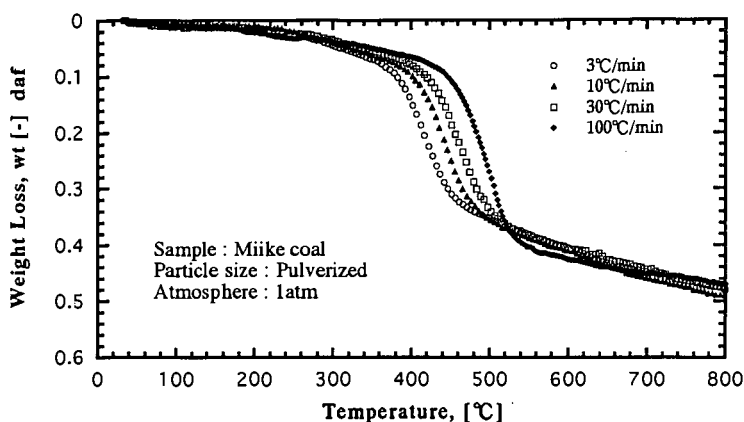


Fig.1 Weight loss curve of Miike coal at atmospheric pressure

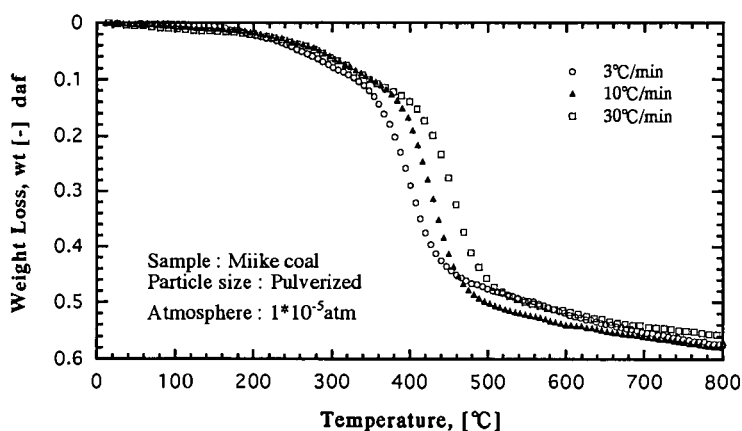


Fig.2 Weight loss curve of Miike coal under vacuum

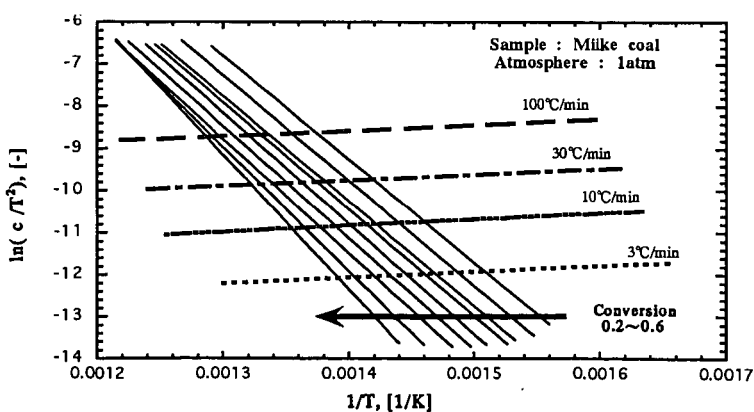


Fig.3 $\ln(c/T^2)$ vs. $(1/T)$ of Miike coal for conversions between 0.2 and 0.6 at atmospheric pressures

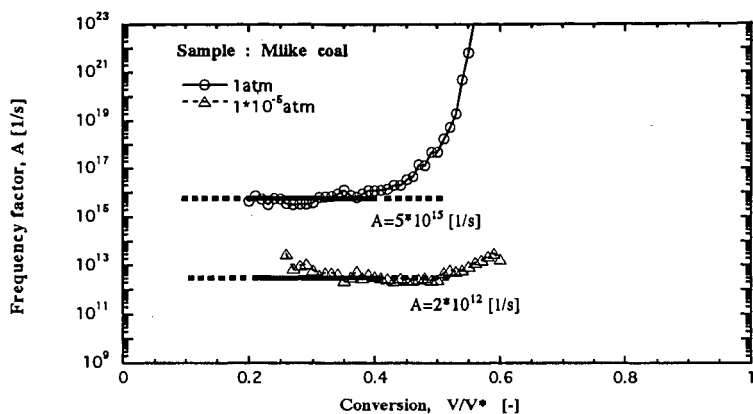


Fig.4 Frequency factor of Miike coal at 0.2-0.6 of the conversion

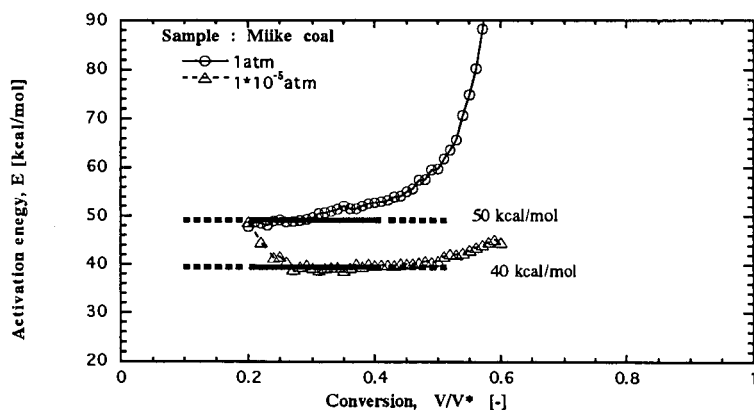


Fig.5 Activation energy of Miike coal at 0.2-0.6 of the conversion

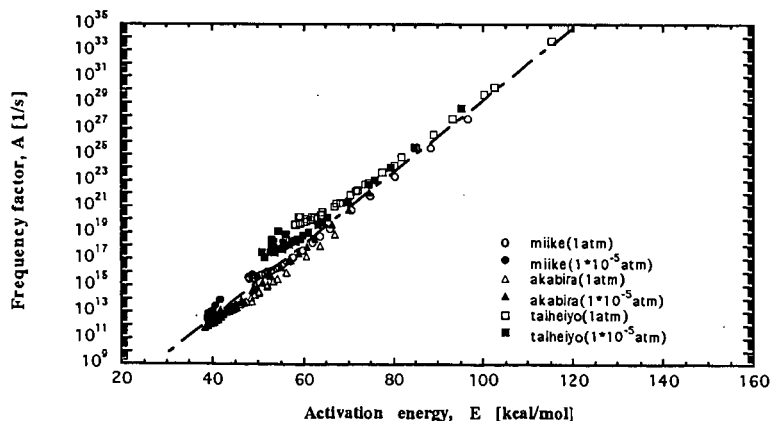


Fig.6 Relationship between frequency factor and activation energy

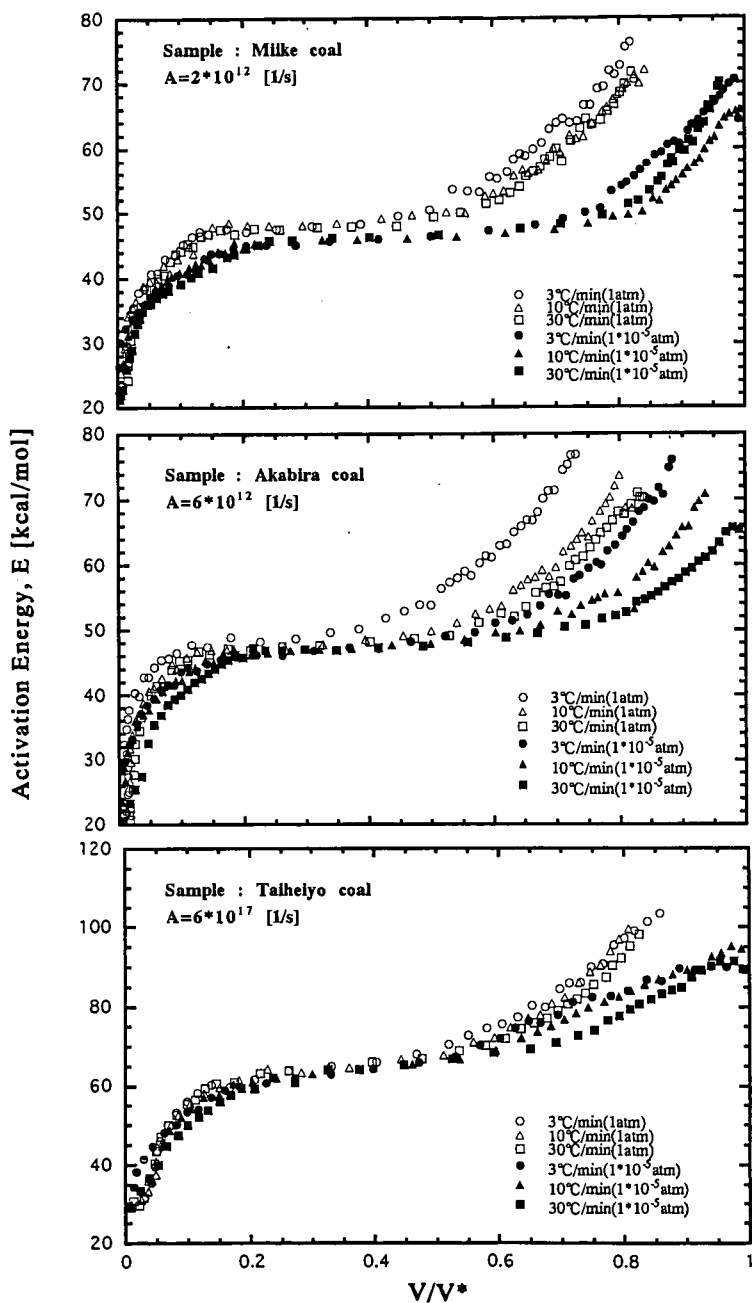


Fig.7 The distribution of activation energy for each coal using a constant frequency factor